



### 저작자표시-비영리-동일조건변경허락 2.0 대한민국

이용자는 아래의 조건을 따르는 경우에 한하여 자유롭게

- 이 저작물을 복제, 배포, 전송, 전시, 공연 및 방송할 수 있습니다.
- 이차적 저작물을 작성할 수 있습니다.

다음과 같은 조건을 따라야 합니다:



저작자표시. 귀하는 원저작자를 표시하여야 합니다.



비영리. 귀하는 이 저작물을 영리 목적으로 이용할 수 없습니다.



동일조건변경허락. 귀하가 이 저작물을 개작, 변형 또는 가공했을 경우에는, 이 저작물과 동일한 이용허락조건하에서만 배포할 수 있습니다.

- 귀하는, 이 저작물의 재이용이나 배포의 경우, 이 저작물에 적용된 이용허락조건을 명확하게 나타내어야 합니다.
- 저작권자로부터 별도의 허가를 받으면 이러한 조건들은 적용되지 않습니다.

저작권법에 따른 이용자의 권리는 위의 내용에 의하여 영향을 받지 않습니다.

이것은 [이용허락규약\(Legal Code\)](#)을 이해하기 쉽게 요약한 것입니다.

[Disclaimer](#)

공학박사학위논문

**Plasma parameter control  
for efficient operation  
of volume produced RF H<sup>-</sup> ion source**

체적 생성 RF 수소 음이온원의 효율적인 운전을 위한  
플라즈마 변수 제어에 관한 연구

2014년 2월

서울대학교 대학원

에너지시스템공학부

정 봉 기

**Plasma parameter control for efficient operation  
of volume produced RF H<sup>-</sup> ion source**

체적 생성 RF 수소 음이온원의 효율적인 운전을  
위한 플라즈마 변수 제어에 관한 연구

지도교수 황 용 석

이 논문을 공학박사 학위논문으로 제출함  
2013년 10월

서울대학교 대학원  
원자핵공학과  
정 봉 기

정봉기의 공학박사 학위논문을 인준함  
2013년 12월

위원장	<u>김 곤 호 (印)</u>
부위원장	<u>황 용 석 (印)</u>
위원	<u>나 용 수 (印)</u>
위원	<u>정 경 재 (印)</u>
위원	<u>정 승 호 (印)</u>

## **Abstract**

# **Plasma parameter control for efficient operation of volume produced RF H<sup>-</sup> ion source**

Bongki Jung

Department of Energy System Engineering

(Nuclear Engineering)

The Graduate School

Seoul National University

In spite of its better stability for long-time operation than the cesiated negative ion source that suffers from difficulty of cesium injection control, the volume-produced RF (radio-frequency) negative ion source still requires further enhancement of current density with lower input RF power and lower operating pressure to satisfy requirements of various applications. In order to increase the volume production of H<sup>-</sup> ions, it is essential to obtain high electron temperature at the driver region while keeping both the electron temperature low below 1 eV and

the electron density as high as possible at the extraction region. Although high electron density with low temperature at the extraction region has been achieved by increasing RF power and adjusting the strength of magnetic filter field, attempts to increase the electron temperature at the driver region with increasing input RF power or changing driving frequency have not yet been proven as efficient. In this study, a new approach based on a particle balance model for hydrogen plasma is suggested to increase the electron temperature effectively in the driver region by reducing the effective plasma size which is defined as the ratio of plasma volume ( $V_p$ ) to effective area ( $A_{eff}$ ).

Measurements with an rf-compensated Langmuir probe show that the electron temperature in the driver region is significantly increased by reducing the length of the discharge chamber due to the reduced effective plasma size. Accordingly,  $H^-$  ion density measurement with laser photo-detachment in the short chamber shows a few times increase compared to the longer one at the same heating power depending on gas pressure. However, the increase drops significantly as operating gas pressure decreases, indicating increased electron temperatures in the extraction region degrade  $H^-$  ion production especially in the low operating pressure regime. Thus, characteristics of the electron temperature in the extraction region for various filter magnet strengths is investigated, and higher  $H^-$  ion density is obtained as decrease of electron temperature with higher magnetic filter field strength in the low pressure regime. Consequently, it is demonstrated that increasing the electron temperature in driver region by adjusting the discharge chamber geometry is efficient to increase  $H^-$  ion production, provided that low electron temperature is maintained with higher filter magnetic strength in the extraction region.

Based on the effects of the effective plasma size and magnetic filter field on plasma parameters, increase of extracted  $H^-$  ion beam current up to 1.45 mA at

RF power of only 0.9 kW (3.2 mA/cm<sup>2</sup>/kW) is definitely achieved with the short chamber length and higher magnetic filter field strength, which is comparable to the highest H<sup>-</sup> current density per unit RF power of the established major volume-produced H<sup>-</sup> ion sources. In addition, it is worth noting that even though measured H<sup>-</sup> ion density decrease in the low operating pressure regime with the short chamber due to higher electron temperature in the extraction region, higher H<sup>-</sup> ion beam current is obtained in the low operating pressure regime from the beam extraction result. This can be explained by further decrease of electron temperature due to the increased  $\int B \cdot dl$  value between the extraction hole and the measurement position considering both filter magnetic field strength and length. This result indicates that high  $\int B \cdot dl$  value is more suitable to suppress electron temperature operating at low pressure regime and with small effective plasma size configuration, since both increasing generation of highly vibrationally molecules in the driver region and lower electron temperature in the extraction region can be satisfied to increase of volume-production of H<sup>-</sup> ions effectively. On the contrary, the electron temperature at the extraction region can be low enough and high electron density can be achieved at high pressure regime. In this operating regime, the main destruction process in transport of the H<sup>-</sup> ions transport in the source region is the mutual neutralization which is increased by higher electron density. Therefore, relatively low  $\int B \cdot dl$  value is more effective to enhance H<sup>-</sup> beam current in considering transport loss of the volume produced H<sup>-</sup> ions in the magnetic filter field region and . Consequently, it is concluded that H<sup>-</sup> ion beam current in the volume-produced H<sup>-</sup> ion source can be optimized depending on the operating pressure regime by not only reducing electron temperature in the extraction region with higher magnetic filter field but also adjusting  $\int B \cdot dl$  value in considering plasma parameters to increase H<sup>-</sup> ion production.

In this dissertation, the discharge chamber and magnetic filter field

configuration as the  $\int B \cdot dl$  value are proposed as critical design parameters from the effects on the RF plasma parameters to increase volume-produced  $H^-$  ion density. Moreover, it has been confirmed that the performance of the volume produced  $H^-$  ion source at a given operating pressure and RF power condition can be optimized by controlling plasma parameters with changing discharge chamber and the  $\int B \cdot dl$  value depending on the operating pressure. The results shown here are expected to be useful to improve the performance of the established volume produced  $H^-$  ion source and extend application fields of  $H^-$  ion source requiring long-time operation.

Keywords: negative hydrogen, ion source, electron temperature, effective plasma size, magnetic filter field,  $H^-$  ion beam extraction

Student number: 2009-30261

# Table of Contents

<b>Abstract</b> .....	i
<b>Table of Contents</b> .....	v
<b>List of Figures</b> .....	vii
<b>List of Tables</b> .....	xi
<b>Chapter 1 Introduction</b> .....	1
1.1 Negative hydrogen ion source .....	1
1.1.1 Applications of Negative hydrogen ion source .....	1
1.1.2 Description of the negative hydrogen ion related particle reactions.....	3
1.2 Necessity of Volume produced negative ion source .....	10
1.3 Previous work and research motivation.....	12
<b>Chapter 2 Particle Balance Model for hydrogen plasma</b> .....	16
2.1 Description of Particle balance model.....	16
2.2 Calculation of electron temperature of the hydrogen plasma .....	19
<b>Chapter 3 Effects of chamber and magnetic filter field configurations on the volume-produced H<sup>-</sup> ion source</b> .....	22
3.1 Experimental setup.....	22
3.1.1 TCP based volume produced H <sup>-</sup> ion source for plasma diagnostics ....	22
3.1.2 Langmuir probe diagnostic.....	24
3.1.3 Laser photo-detachment diagnostics .....	27
3.2 Effects of various chamber lengths on characteristics of plasma parameters and H <sup>-</sup> ion production .....	31
3.2.1 Characteristics of plasma parameters for change of chamber length.....	31
3.2.2 H <sup>-</sup> ion production for change of chamber length .....	35
3.3 Effects of various magnetic filter field strengths on characteristics of plasma parameters and H <sup>-</sup> ion production.....	39
3.3.1 Characteristics of plasma parameters for change of magnetic filter field	

strength .....	39
3.3.2 H <sup>-</sup> ion production for change of magnetic filter field strength.....	42
<b>Chapter 4 Extraction of H<sup>-</sup> ion beam for various chamber and magnetic filter field configurations .....</b>	<b>47</b>
4.1 Experimental setup .....	47
4.1.1 H <sup>-</sup> ion beam extraction system .....	48
4.1.2 Measurement of H <sup>-</sup> ion beam: Faraday cup.....	49
4.2 Characteristics of H <sup>-</sup> ion current for change of chamber length.....	50
4.3 Analysis of correlation between extracted H <sup>-</sup> ion beam current and measured H <sup>-</sup> ion density.....	53
4.3.1 Neutralization of H <sup>-</sup> ion in the beam extraction region.....	53
4.3.2 Effects of $\int B \cdot dl$ value in the H <sup>-</sup> ion source region.....	56
<b>Chapter 5 Summary and Conclusions .....</b>	<b>67</b>
<b>References.....</b>	<b>70</b>
<b>Abstract in Korean .....</b>	<b>72</b>

## List of Figures

<b>Figure 1.1</b>	The neutralization efficiency at optimum gas thickness as functions of beam energy and comparing between experimental and calculation results.....	3
<b>Figure 1.2</b>	Reaction branches of H <sup>-</sup> ion production process.....	4
<b>Figure 1.3</b>	Cross sections for the formation of vibrational excited molecules H <sub>2</sub> (v'' = 1 ~ 14), vs electron energy for electrons impinging on ground-state (v'' = 0) molecules.....	6
<b>Figure 1.4</b>	Dissociative attachment cross sections for the formation of H <sup>-</sup> ion vs electron energy for vibrational excited states molecules.....	8
<b>Figure 1.5</b>	Reaction rates of destruction processes with H <sup>-</sup> ion.....	10
<b>Figure 1.6</b>	The typical extracted H <sup>-</sup> ion current density of prototype RF H <sup>-</sup> ion source for ITER NNBI for different operating pressure inside the source .....	11
<b>Figure 1.7</b>	Schematic figure of surface produced negative ion source and disadvantages of the source .....	11
<b>Figure 1.8</b>	(a) conceptual schematic figure and (b) drawing of the TCP based volume produced H <sup>-</sup> ion sources at Seoul National University. ....	13
<b>Figure 1.9</b>	Results of electron temperature measurement for dependency of electron temperature on (a) input RF power & (b) driving frequency.....	14
<b>Figure 2.1</b>	Rate coefficients of reaction processes vs. the electron temperature T <sub>e</sub> ....	17
<b>Figure 2.2</b>	Particle balance equations for hydrogen plasma .....	17
<b>Figure 2.3</b>	Calculated electron temperature of hydrogen plasma for various effective plasma size and neutral gas density. ....	21
<b>Figure 3.1</b>	Two discharge chambers with different lengths to investigate the change of plasma parameters for the different effective plasma size.....	22
<b>Figure 3.2</b>	Langmuir probe and laser photo-detachment diagnostic system to measure plasma parameters .....	23

<b>Figure 3.3</b>	(a) Schematic diagram of Langmuir probe and circuitry, (b) a typical current-voltage (I-V) curve of Langmuir probe, (c) 1st derivative of the I-V curve and determination of plasma potential, and (d) semi-log plot of the I-V curve and linear fit to find electron temperature.....	25
<b>Figure 3.4</b>	Comparison of measured laser photo detachment diagnostic signal in (a) prototype RF ion source for ITER NNBI and (b) TCP based H <sup>-</sup> ion source.....	29
<b>Figure 3.5</b>	Saturation of LPD signal for laser power density.....	30
<b>Figure 3.6</b>	Validation of $n_{H^-}/n_e$ ratio for various probe bias voltage.....	30
<b>Figure 3.7</b>	Measured electron temperature with various input RF power for change of chamber length .....	33
<b>Figure 3.8</b>	Measured electron temperature and comparison with the results of particle balance model.....	33
<b>Figure 3.9</b>	Electron density with various operating pressure and input RF power for change of chamber length.....	34
<b>Figure 3.10</b>	Measured electron (a) temperature and (b) density in the H <sup>-</sup> extraction region with various input RF power for change of chamber length. ....	37
<b>Figure 3.11</b>	Characteristics of measured H <sup>-</sup> ion density with various pressure and input RF power for change of chamber length .....	38
<b>Figure 3.12</b>	Measurement of negative ion density for various magnetic filter field configurations.....	39
<b>Figure 3.13</b>	Measured electron (a) density and (b) temperature with various magnetic filter field strengths for change of chamber length.....	41
<b>Figure 3.14</b>	Measured H <sup>-</sup> ion density for various magnetic filter field configurations in (a) long and (b) short chamber length configurations .....	44
<b>Figure 3.15</b>	Increasing rate of H <sup>-</sup> ion density for various filter magnetic field strengths with the same increased RF input power in (a) long and (b) short chamber	

	length configuration.....	45
<b>Figure 3.16</b>	Increasing rate of electron density for various filter magnetic configuration with the same increased RF input power.....	46
<b>Figure 4.1</b>	Drawing of TCP H <sup>-</sup> ion source with change of effective plasma size.....	48
<b>Figure 4.2</b>	A schematic drawing of the Faraday cup.....	49
<b>Figure 4.3</b>	Extracted H <sup>-</sup> ion beam current for different effective plasma size with various operating pressure and RF power .....	52
<b>Figure 4.4</b>	Estimation of residual gas pressure in the H <sup>-</sup> ion beam transport .....	53
<b>Figure 4.5</b>	Neutralization loss ratio for various background gas pressure .....	54
<b>Figure 4.6</b>	Neutralization loss ratio in the beam extraction and transport region of TCP based RF H <sup>-</sup> ion source .....	54
<b>Figure 4.7</b>	Modified H <sup>-</sup> ion density in consideration of neutralization loss in the H <sup>-</sup> ion beam transport .....	55
<b>Figure 4.8</b>	Calculated axial transverse magnetic field profile in the source region ...	58
<b>Figure 4.9</b>	Characteristics of electron temperature for various $\int B \cdot dl$ value with (a) long chamber, (b) short chamber configuration.....	59
<b>Figure 4.10</b>	Characteristics of electron density for various $\int B \cdot dl$ value with(a) long chamber, (b) short chamber configuration.....	59
<b>Figure 4.11</b>	H <sup>-</sup> ion density increasing ratio for various $\int B \cdot dl$ value with (a) long chamber (b) short chamber.....	60
<b>Figure 4.12</b>	Increase rates of H <sup>-</sup> ion density for the reduction of electron temperature	61
<b>Figure 4.13</b>	Estimation of H <sup>-</sup> ion density near the extraction hole region.....	61
<b>Figure 4.14</b>	Calculated mean free path for H <sup>-</sup> ion destruction reactions .....	64
<b>Figure 4.15</b>	Calculated mean free path for total H <sup>-</sup> ion destruction reactions .....	64
<b>Figure 4.16</b>	Comparison of e <sup>-</sup> /H <sup>-</sup> ratio between the results from the H <sup>-</sup> ion beam current and measured H <sup>-</sup> ion density. ....	65
<b>Figure 4.17</b>	Comparison with H <sup>-</sup> ion beam current and modified H <sup>-</sup> ion density in	

considering additional  $H^-$  production and destructions ..... 66

## List of Tables

<b>Table 1.1</b>	The characteristics of some major negative ion sources.....	12
<b>Table 1.2</b>	The reaction processes considered in the hydrogen plasma model. ....	16

# Chapter 1 Introduction

## 1.1 Negative hydrogen ion source

Negative hydrogen ( $H^-$ ) ion sources have been widely used for a primary particle source of proton accelerators to investigate high energy nuclear physics [1] and the high energy neutral beam injection system for the magnetized fusion plasma heating [2]. However,  $H^-$  ion generally has a rare production rate in the hydrogen plasma. Therefore, research on increase of  $H^-$  production rate is still required for the higher efficiency of the negative hydrogen ion source applications.

### 1.1.1 Applications of Negative hydrogen ion source

#### ➤ Circular accelerators

Circular proton accelerators such as cyclotron and synchrotron are extensively used for from medical applications [3] to high energy particle physics.[1] Circular accelerators are utilized by closed circular orbit of charged particle trajectory in vertical magnetic field where high kinetic energy can be achieved with relatively low accelerating voltage. However, circular accelerators has difficulty of injection of charged particles into the accelerator or extraction of accelerated particles from the accelerator due to the vertical magnetic field incompatibly. To solve this problem, the negative hydrogen ion is used for the circular proton accelerator. When using a thin foil target into the particle orbit,  $H^-$  ions lose electrons at the target and are changed into protons. As a result, the

curvature of accelerated particle trajectories in a magnetic field reverses and the  $H^-$  ions easily inject to or escape from the accelerator.

➤ Tandem accelerator

Due to simple particle acceleration process, electrostatic accelerators are still used for applications such as material analysis, modification and radiation production [4], but basically, electrostatic acceleration is limited by high voltage insulation of acceleration stages. To improve the intrinsic limitation of electrostatic accelerators, tandem accelerator was developed to obtain higher beam energy than with single ended electrostatic accelerator. The charge exchange of negative ions into positive ions enable twice acceleration in the drift tube with a single bias voltage and obtain twice kinetic energy for the accelerating voltage. Therefore, negative ion injection into the drift tube is a key point of tandem accelerator.

➤ Neutral beam injector

Neutral beam injection (NBI) system is an efficient external heating device to deliver heating power into the magnetized fusion plasma. Generally, NBI system is based on the positive ion source which has higher current density than the negative ion source, but positive ion based NBI has limitation of increasing neutral beam energy, due to lower neutralization efficiency of the positive ion with above 100keV/amu beam energy. While the efficiency of the negative ion still maintains more than 50% in spite of 1 MeV/amu. Fig. 1 shows calculated neutralization efficiency by using charge exchange cross-section of the both ions experimental result of neutralization efficiency of negative ion based NBI system.

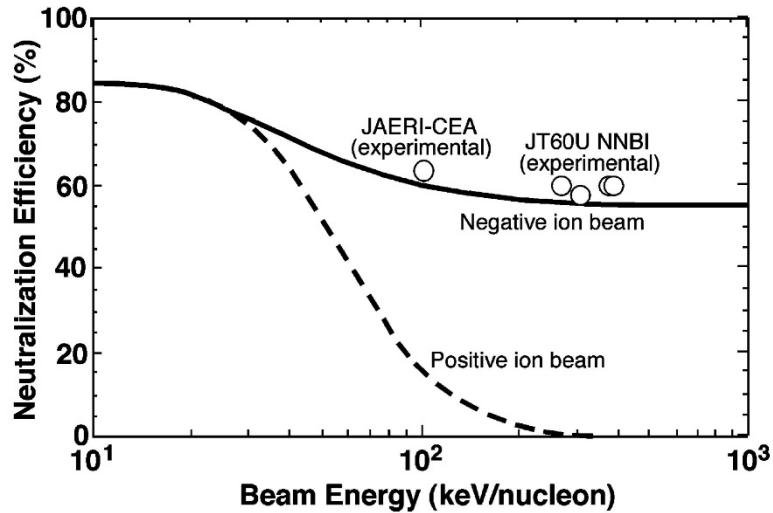


**Figure 1.1 The neutralization efficiency at optimum gas thickness as functions of beam energy and comparing between experimental and calculation results.[6]**

Accordingly, the large size fusion plasma device essentially require negative ion source based NBI system such as JT60U, ITER since higher energetic neutral beam (>several hundred of keV) can penetrate enough into the plasma and deposit the beam power on the core of the plasma.[2,5-9]

### 1.1.2 Description of the negative hydrogen ion related particle reactions

Basically, production process of  $H^-$  ions are classified in two types [10,11], surface and volume process. In the surface process, the  $H^-$  ion is produced on the wall surface from two particle sources. They are hydrogen atoms and positive ions ( $H^+$ ,  $H_2^+$ ,  $H_3^+$ ) which can convert into  $H^-$  ion directly, when they collide with the wall surface. On the other hand, in the volume process, the  $H^-$  ions are produced in the plasma volume region through two different electron-molecule collision processes which are excitation process of molecules to the higher vibrational state

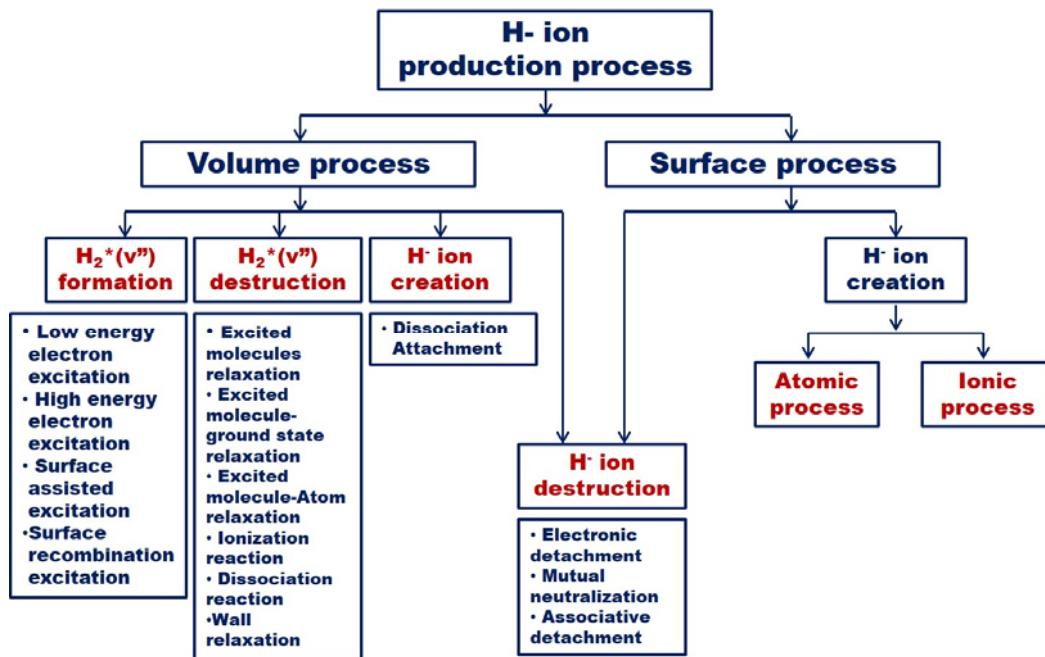


Figure 1.1 Reaction branches of H<sup>-</sup> ion production process.[12]

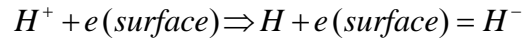
with higher energy electrons and dissociative attachment with lower energy electrons.

Based on these two production processes, reaction branches of related particles for H<sup>-</sup> production and destruction processes are summarized in Fig. 2, and more details of reactions are described below.

➤ Surface production of negative hydrogen ion

The surface production of H<sup>-</sup> ion is established on tunneling effect of the electron from the surface to the H atom which is emitting from the surface [11]. Therefore, the hydrogen atom collides with the wall having low work-function and is changed into H<sup>-</sup> ion. In addition, hydrogen ions (H<sup>+</sup>, H<sub>2</sub><sup>+</sup>, H<sub>3</sub><sup>+</sup>) are also re-emitted as H<sup>-</sup> from a surface with low work-function when it impact that wall with higher

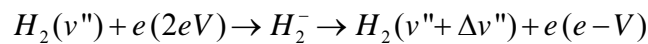
velocities.



Consequently, surface production of  $H^-$  ion highly depends on the work function of the convertor surface. An increase of the negative ion beam current by a factor of 500 with a molybdenum convertor surface with lowering the work function by 2.9 eV has been reported.[13] Enhanced performance of the negative ion source by adding small amounts of cesium during operation has also been observed.[14] Thus, control of cesium layer on the surface is highly required to reduce work function of converting surface for a higher surface  $H^-$  production.

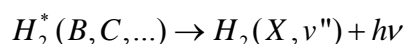
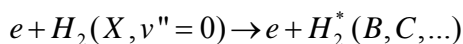
➤ Volume production of negative hydrogen ion

Higher volume  $H^-$  ion production requires two processes in the plasma volume region [10,15,16]. First, formation of higher vibrationally excited molecules by higher energy electrons. Second, dissociative attachment process of vibrationally excited molecules with lower energy electrons. Vibrational excitation of molecules in collision with low energy electrons (<5eV) through the  $H_2^-$  resonant state(denoted e-V excitation)



is very effective in changing the vibrational state, but the most probable change in  $v''$  is  $\Delta v'' = \pm 1$ , so high collision rate would be required to significantly populate the vibrationally excited molecules spectrum. The e-V excitation is responsible for vibrational excitation of hydrogen molecules up to  $v'' = 4$  only. Reaction rate for this reaction is  $\langle \sigma v \rangle \approx 2 * 10^{-15} \text{ m}^3\text{s}^{-1}$  for  $v'' = 0$  to 1. The reaction rates for every higher  $v''$  are reduced nearly one order. [15] The high energy electron excitation

(E-V) reaction process is the main reaction which are most important for H- ion formation through volume production process. Through E-V excitation, the higher vibrational states can be populated by radiative decay from singlet states, excited by collisions of ground state molecules with energetic electrons:



The electron excitation cross sections from an initial level,  $v'' = 0$ , to a final level,  $v''$  were calculated by Hiskes, as shown in fig. 1. 3. The E-V excitation is efficient when the electron energy exceeds approximately 20eV.[12,15-17]

The vibrationally excited  $H_2(v'')$  molecules are destroyed or relaxed to lower vibrational levels by many processes.[12,18-23]

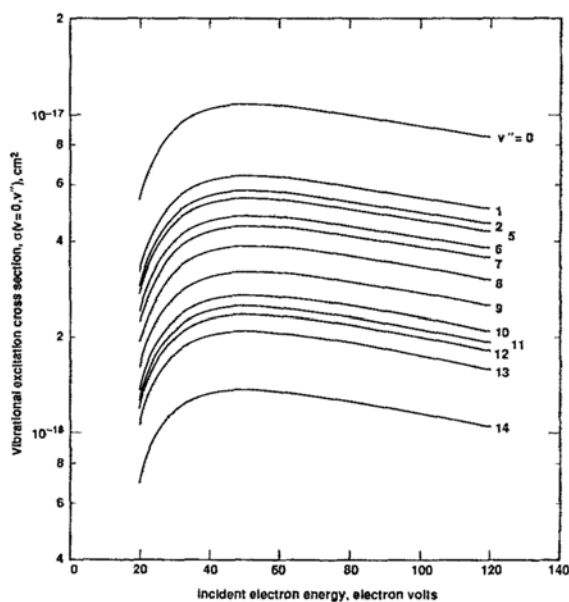
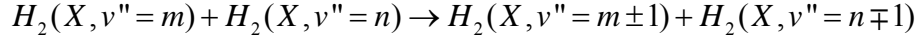
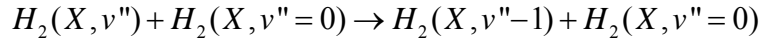


**Figure 1.2 Cross sections for the formation of vibrational excited molecules  $H_2(v'' = 1 \sim 14)$ , vs electron energy for electrons impinging on ground-state ( $v'' = 0$ ) molecules.[17]**

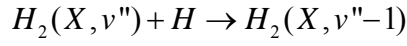
-Excited molecule-excited molecules relaxation (V-T)



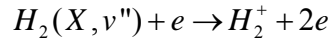
-Excited molecule-ground state molecules relaxation (V-V)



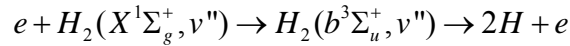
-Excited molecule-atom relaxation (V-t)



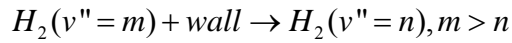
-Ionization reaction



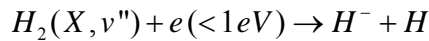
-Dissociation reaction



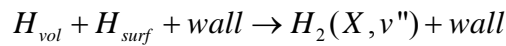
-Wall relaxation



-Dissociative attachment



In addition to e-V and E-V process, plasma-wall interaction can contribute to the production of vibrationally excited molecules by the recombination of molecular ions on the wall surface.[24]



This process relies on the Auger neutralization of molecular hydrogen ions  $H_2^+$  and  $H_3^+$  on the wall and creates all possible vibrationally excited  $H_2$  molecules

from  $v'' = 0$  to 14.

In presence of high concentration of vibrationally excited hydrogen molecules, generation of  $H^-$  ions are generally understood as the consequence of dissociative attachment process.



The low energy electrons dissociatively combine with vibrationally excited hydrogen molecules and form  $H^-$  ions. Dissociative attachment to vibrationally cold  $H_2$  ( $v''=0$ ) molecules is known to have a very small cross section ( $10^{-21} \text{cm}^2$ ). However, it was shown that dissociative attachment cross section increase when the hydrogen molecules are vibrationally excited by experimental and theoretical calculation. The DA cross section increases by five orders of magnitude when the hydrogen molecules are vibrationally excited from  $v''=0$  to 5 and stay constant at

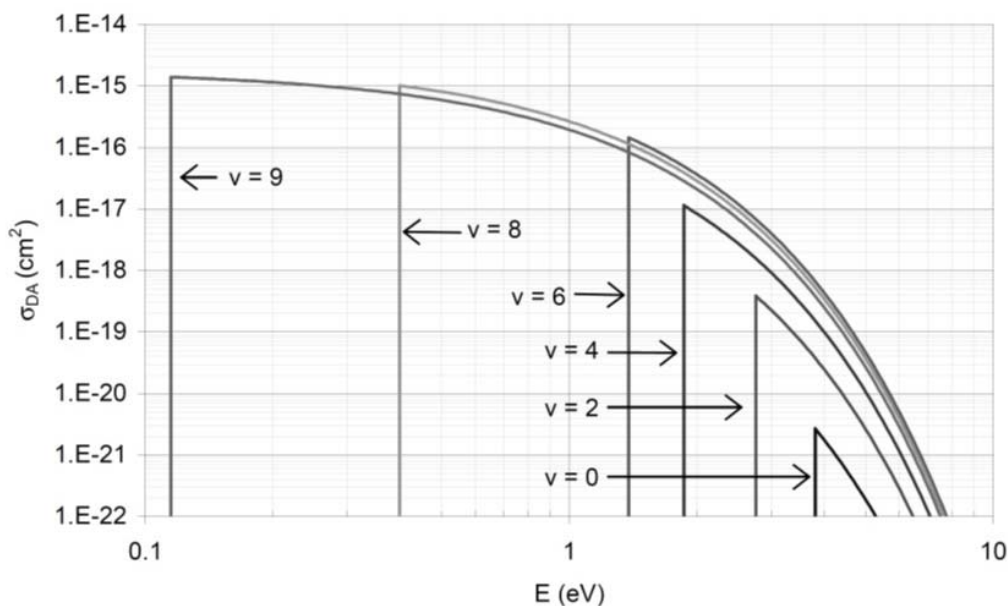


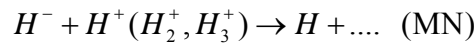
**Figure 1.3 Dissociative attachment cross sections for the formation of  $H^-$  ion, vs electron energy for vibrational excited states molecules.[12]**

higher  $v''$ . The optimum electron energies are near their threshold ( $\sim 0.5 \sim 1 \text{ eV}$ ), and the threshold energy goes down when  $v''$  goes up, as shown in fig. 1. 4. Thus low energy electrons can be very effective in generating  $\text{H}^-$  ions by DA to highly vibrationally excited molecules. The calculated rate constant for dissociative attachment is presented in fig. 1. 4. Dissociative attachment reaction is the most desirable reaction in the extraction region because in a volume  $\text{H}^-$  ion source, approximately 90% of the negative ions are generated from the  $\text{H}_2$  ( $14 \geq v'' \geq 5$ ) molecules through this process.

➤ Destruction of negative hydrogen ion

$\text{H}^-$  ions are also destroyed by many process, but three volume destruction process are most important as shown in Fig. 1. 5. [12,15,16,25]

-Mutual neutralization (MN) in collision with positive ions:



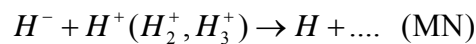
$$\langle \sigma v \rangle = \sim 5 \times 10^{-14} \text{ m}^3/\text{s}$$

-Electron detachment (ED) in collision with electrons:



$$\langle \sigma v \rangle = \sim 2 \times 10^{-14} \text{ m}^3/\text{s} (\sim 1.5 \text{ eV}), \sim 1 \times 10^{-12} \text{ m}^3/\text{s} (\sim 30 \text{ eV})$$

-Associative detachment (AD) in collision with atoms:



$$\langle \sigma v \rangle = \sim 10^{-15} \text{ m}^3/\text{s}$$

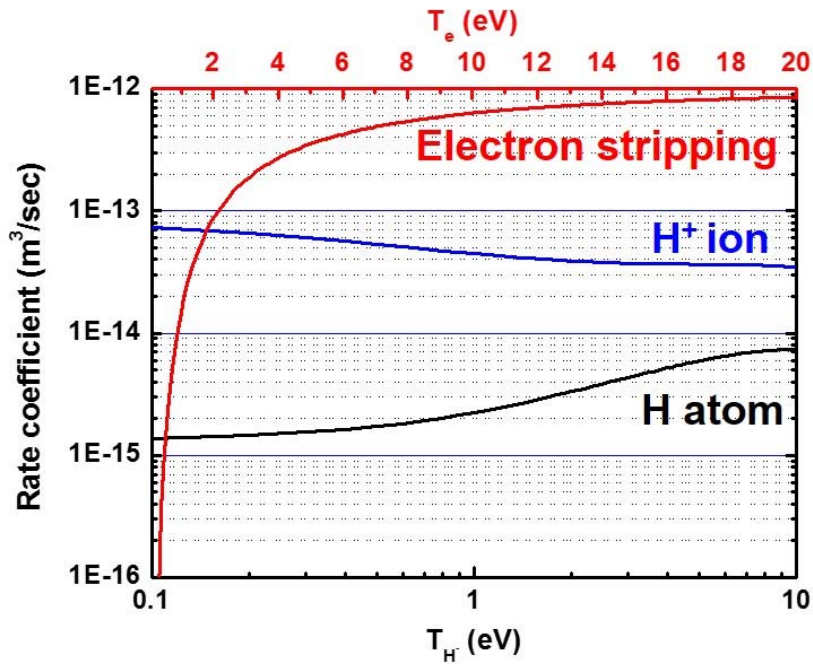


**Figure 1.4 Reaction rates of destruction processes with H<sup>-</sup> ion.[12]**

Among the H<sup>-</sup> ion destruction processes the most important one is mutual neutralization. The electron detachment can be reduced by lowering the density of energetic electrons.

## 1.2 Necessity of Volume produced negative ion source

H<sup>-</sup> ion source generally requires lower operating pressure to reduce the electron stripping loss in the H<sup>-</sup> beam extraction and acceleration regions. For example, operating pressure of the ion source for ITER negative ion based NBI system is limited by 0.3Pa (2.3mTorr). Thus, surface produced H<sup>-</sup> ion source with cesium injection is commonly used due to higher H<sup>-</sup> production rate compared to volume produced H<sup>-</sup> ion source in lower operating pressure regime as shown in Fig. 1. 6. [26] However, stable operation of H<sup>-</sup> ion source is also required to increase

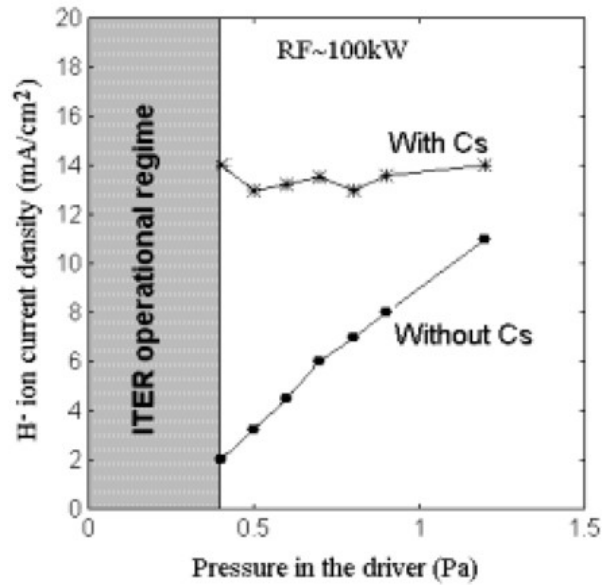


Figure 1.6 The typical extracted H- ion current density of prototype RF H- ion source for ITER NNBI for different operating pressure inside the source.[26]

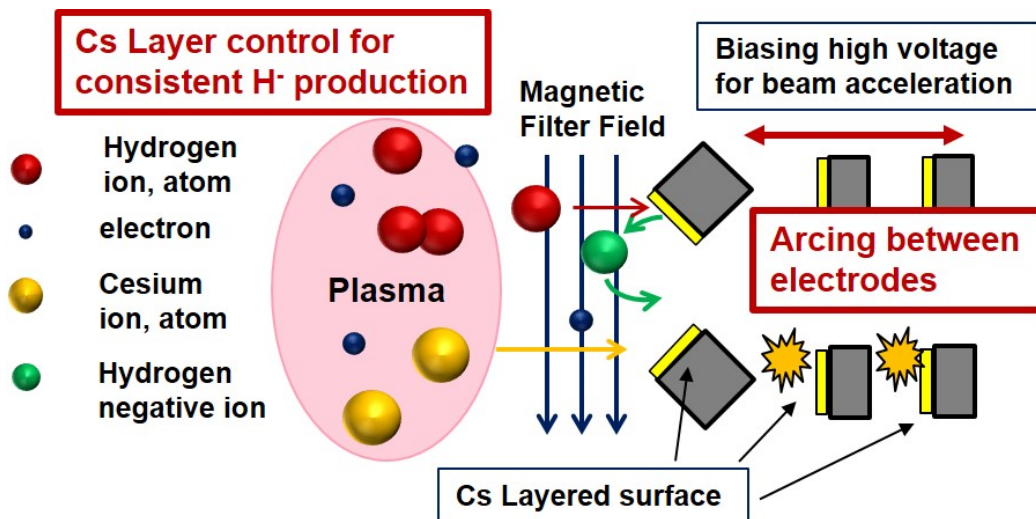


Figure 1.7 Schematics of surface produced negative ion source and disadvantages of the source.

efficiency of the source applications besides H<sup>-</sup> production rate. In this point of view, the volume-produced H<sup>-</sup> ion sources show better stability for long-time operation, compared to the cesiated surface produced H<sup>-</sup> ion source that suffers from difficulty of cesium injection control and high-voltage arcing by deposition of cesium on acceleration electrodes as depicted in Fig. 1. 7. [1,2,15,16] Consequently, enhancement of beam current density in volume produced H<sup>-</sup> ion source with lower input power and lower operating pressure is still required to the applications such as proton accelerators and neutral beam injectors in a continuous-wave (CW) operation mode.

### 1.3 Previous work and research motivation

Since the discovery in 1977 of the volume production mechanism attributed to dissociative electron attachment of low energy electrons to vibrationally excited molecules, various types of volume produced H<sup>-</sup> ion sources has been developed and studied. As shown in table 1.1. volume negative ion sources operating in accelerators with H<sup>-</sup> ion density in the 100 mA/cm<sup>2</sup> range opens the prospect of creating volume cesium-free sources for fusion.[15,16] However, efficient volume negative ion production with lower RF power density still needs to be studied for the success of volume negative ion source.

	Operation Type	Total Current (Input Power)	Current Density	Power Efficiency
NNBI for ITER	Cs seeded (Pulse[~1ms])	60A(CW) (800kW)	30mA/cm <sup>2</sup>	Large scale multi-holes
SNS	Cs seeded (Pulse[~1ms])	55 mA (60kW)	195 mA/cm <sup>2</sup>	3.2 mA/cm <sup>2</sup> /kW
DESY	Volume (Pulse[~100μs])	40mA (40kW)	141 mA/cm <sup>2</sup>	3.5 mA/cm <sup>2</sup> /kW
SNU	Volume (CW)	1.4mA (1.4kW)	3 mA/cm <sup>2</sup>	2.5 mA/cm <sup>2</sup> /kW

**Table 1. 1 The characteristics of some major negative ion sources.**

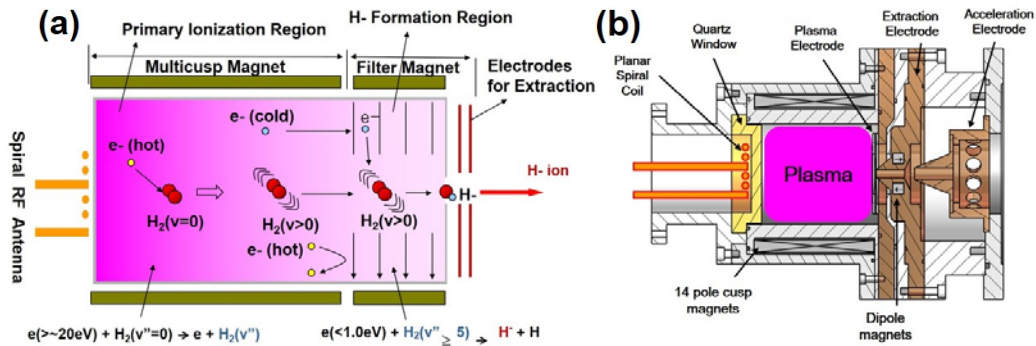


**Figure 1.8 (a) Conceptual schematic figure and (b) drawing of the TCP based volume produced H- ion sources at Seoul National University**

Among these volume-produced ion sources, a tandem type volume-produced H- ion source based on transformer-coupled plasma (TCP) with external antenna and multi-cusp configuration has been developed and characterized to be operating in a long-lifetime, CW mode without cesium at Seoul National University (SNU).[27] Fig.1.8 shows conceptual design and system drawing of the H- ion source. In the TCP based volume produced H- ion sources, H- ions are generated by dissociative attachment of low energy electrons to vibrationally-excited molecules in front of an extraction aperture. The vibrationally-excited molecules are generated through collisions with fast electrons in plasma heating region, near the external RF antenna. Therefore, appropriate control of electron temperature between the heating region and the extraction region is essential to obtain high H- ion current in volume-produced H- ion sources. While lowering electron temperature in the extraction region has been successfully accomplished by utilizing magnetic filter field in front of the extraction aperture, [27] As shown in Fig. 1. 9, attempts to increase the electron temperature in the heating region with various techniques such as changing driving frequency [28] and increasing input rf power have not yet been proven as efficient.[27]

In this research, a simple method is suggested to increase the electron

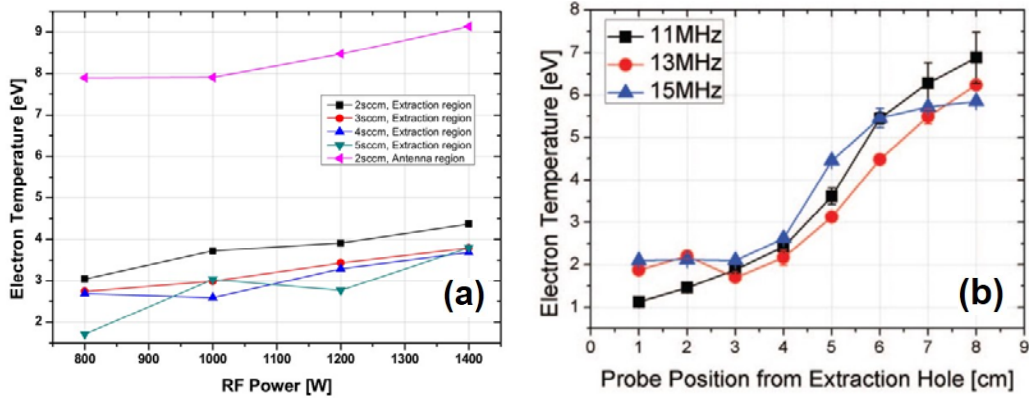


**Figure 1.9 Results of electron temperature measurement for dependency of electron temperature on (a) input RF power & (b) driving frequency.**

temperature in the driver region by reducing the length of a discharge chamber such that the effective plasma size, which is defined as the ratio of plasma volume ( $V_p$ ) to effective area ( $A_{eff}$ ), is reduced. From a simple particle balance for electrons in which the generation of electrons through ionization collisions with background neutral molecules is balanced with the loss across a surrounding sheath with an effective loss area, one can easily recognize that the electron temperature is inversely proportional to the product of neutral density ( $n_g$ ) and effective plasma size ( $d_{eff}$ ) through the following nonlinear equation [29]

$$\frac{K_{iz}(T_e)}{u_B(T_e)} = \frac{1}{n_g d_{eff}} \quad (1)$$

where  $K_{iz}$  and  $u_B$  is the rate constant for electron impact ionization and the Bohm speed, respectively. Note that both numerator and denominator of left-hand-side of Eq. (1) are function of the electron temperature  $T_e$ . According to the above simple calculation, effects of  $d_{eff}$  on plasma parameters ( $n_e, T_e$ ),  $H^-$  production and characteristics of  $H^-$  ion beam current is clarified for various chamber configurations.

This paper is organized as follows. Chapter 2 is devoted to describe the particle balance model to determine characteristics of  $T_e$  in hydrogen plasma with respect to various plasma parameters and external conditions. In chap. 3, the detailed experimental setup and diagnostics of plasma parameters are presented, and characteristics of  $H^-$  ion density are analyzed with various plasma parameters for different discharge chamber lengths and magnetic filter field configurations. Based on this result, characteristics of  $H^-$  beam extraction for various chamber configurations will be discussed and correlation between extracted  $H^-$  ion beam current and measured  $H^-$  ion density is analyzed in chap. 4. Overall conclusions of the present research and future work are contained in Chap. 5.

## Chapter 2 Particle Balance Model for hydrogen plasma

In this chapter, results of particle balance model for hydrogen plasma are presented to estimate characteristics of electron temperature which is the first requirements for efficient volume production of  $H^-$  for a given operating pressure and effective plasma size conditions.

### 2.1 Description of Particle balance model

The simple particle balance model which was originally developed to estimate the fraction of ion species in hydrogen discharges has been modified to take the effects of chamber geometry on the electron temperature. The reaction processes

Cross section	Reaction Process
$\sigma_1$	$H + e \rightarrow H^+ + 2e$
$\sigma_2$	$H_2 + e \rightarrow H_2^+ + 2e$
$\sigma_3$	$H_2 + e \rightarrow 2H + e$
$\sigma_4$	$H_2^+ + e \rightarrow 2H$
$\sigma_5$	$H_2^+ + e \rightarrow H + H^+ + e$
$\sigma_6$	$H_2^+ + H_2 \rightarrow H_3^+ + H$
$\sigma_7$	$H_3^+ + e \rightarrow H + H_2$
$\sigma_8$	$H_3^+ + e \rightarrow 2H + H^+ + e$

Table 1.1 The reaction processes considered in the hydrogen plasma model

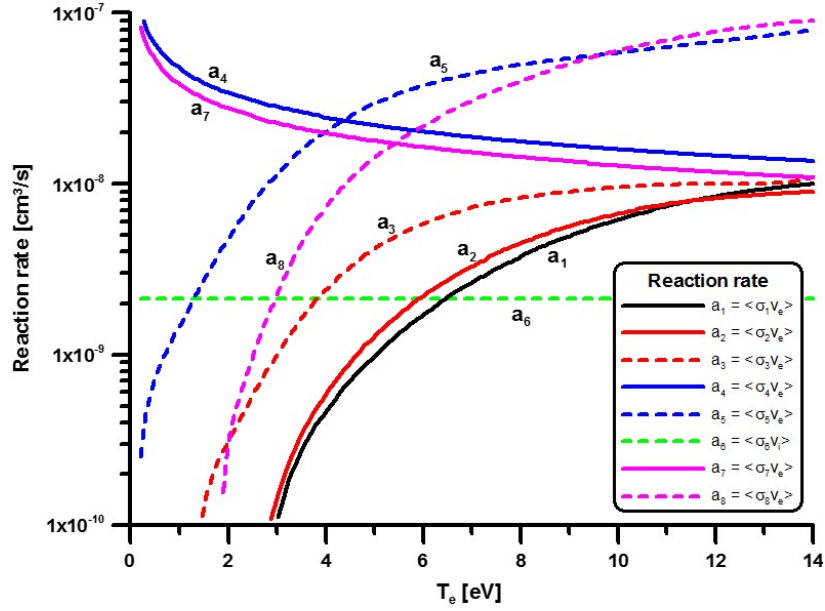


Figure 2.1 Rate coefficients of reaction processes vs. the electron temperature  $T_e$

Particle balance equation

$$\begin{aligned}
 H(N_1) \quad & 2N_2n_e a_3 + 2n_2n_e a_4 + n_2n_e a_5 + n_2N_2 a_6 + n_3n_e a_7 + 2n_3n_e a_8 + (n_1/\tau_1(T_e)) + (n_3/\tau_3(T_e)) \\
 & - N_1n_e a_1 - g(N_1/T_1) = 0 \\
 H_1^+(n_1) \quad & N_1n_e a_1 + n_2n_e a_5 + n_3n_e a_8 - (n_1/\tau_1(T_e)) = 0 \\
 H_2^+(n_2) \quad & N_2n_e a_2 - n_2n_e a_4 - n_2n_e a_5 - n_2N_2 a_6 - (n_2/\tau_2(T_e)) = 0 \\
 H_3^+(n_3) \quad & n_2N_2 a_6 - n_3n_e a_7 - n_3n_e a_8 - (n_3/\tau_3(T_e)) = 0
 \end{aligned}$$

Charge conservation equation

$$n_1 + n_2 + n_3 = n_e$$

Particle conservation equation

$$N_2 + (1/2)N_1 + (1/2)n_1 + n_2 + (3/2)n_3 = p/(k_B T_0)$$

$\tau_i(T_e)$ : containment time for each ion species for electron temperature ( $i=1, 2, 3$ )  
 $T_1$ : transit time of H atoms across the chamber ( $= 4(V/A)/v_0$ )  
 $\gamma$ : recombination factor for H atoms at the wall  
 $V/A$ : volume to surface ratio of the source chamber  
 $p$ : hydrogen gas pressure  
 $v_0$ : mean velocity of H atoms

Unknown:  $N_1, N_2, n_1, n_2, n_3, T_e$   
 Given:  $V/A, v_0, T_g, \tau_1, \tau_2, \tau_3, g$   
 Variable:  $n_e, p$

Figure 2.2 Particle balance equations for hydrogen plasma

considered in the model are in table 2. 1. [12] This model assumes that a Maxwellian plasma is produced and that electrons play a dominant role on ionization or dissociation of the hydrogen species. The variation of rate coefficients with the electron temperature  $T_e$  is represented in Fig. 2. 1. According to CW operation of the experimental condition, steady-state hydrogen plasma is considered, and the detailed particle balance equations for hydrogen plasma and its notation presented in Fig. 2. 2.

where  $n_H$ ,  $n_{H_2}$ ,  $n_1$ ,  $n_2$  and  $n_3$  are the densities of H atoms, H<sub>2</sub> molecules, H<sup>+</sup> ions, H<sub>2</sub><sup>+</sup> and H<sub>3</sub><sup>+</sup> molecular ions, respectively,  $\tau_1$ ,  $\tau_2$  and  $\tau_3$  are the containment times of H<sup>+</sup> ions, H<sub>2</sub><sup>+</sup> and H<sub>3</sub><sup>+</sup> molecular ions,  $T_1$  is the transit time of H atoms across the chamber, and the containment time of atoms would be  $T_1/\gamma$ ,  $\gamma$  is either the recombination factor for H atoms at the wall (stainless steel=0.1),  $N_0 = p/(k \cdot T_g)$ , with  $p$  = hydrogen gas pressure,  $k$  = Boltzmann's constant,  $T_g$  = gas temperature,  $n_0$  is the density of hydrogen molecules before discharge,  $n_e$  is the density of electrons. In the above equations, all the species of ions recombine at the wall to produce molecules. However the loss rate of H atoms equals  $\gamma N_1/T_1$  and H atoms only partially recombine when  $\gamma$  is smaller than unity. The value of  $T_1$  is calculated from the relation  $T_1 = 4(V/(v_0A))$ , where  $V$  is the volume of the source chamber,  $A$  the surface area of the chamber wall and  $v_0$  the mean velocity of H atoms. It is assumed that  $T_g = 1000K$ ,  $T_H = 0.1$  eV [30].

Unlike the original model, in this particle balance model, the electron temperature is treated as an unknown parameter through the modification of ion transit time as

$$\tau_{H^+} = \left( \frac{V}{A_{eff}} \right) \sqrt{\frac{M}{kT_e}}$$

where  $M$  is the mass of hydrogen atom,  $k$  is the Boltzmann constant, and  $T_e$  is the electron temperature in kelvin. Ion transit times for other species such as H<sub>2</sub><sup>+</sup> and

H<sub>3</sub><sup>+</sup> are also replaced as above equation with their own masses. For a cylindrical plasma chamber with radius R and length, the expression for the effective area is

$$A_{eff} = 2\pi R(\alpha Lh_R + Rh_L)$$

where

$$h_L = 0.86 \left( 3.0 + \frac{L}{2\lambda_i} \right)^{-1/2} \quad h_R = 0.8 \left( 4.0 + \frac{R}{\lambda_i} \right)^{-1/2}$$

are the sheath to bulk density ratios of the positive ion species as calculated by Godyak [29,30] for an electropositive plasma in a low-pressure regime, for parallel-plate (h<sub>L</sub>) and infinite cylinder (h<sub>R</sub>) geometries, respectively. The positive ion mean free path is taken to be

$$\lambda_i = \frac{1}{n_{neu} \sigma_i}$$

with  $\sigma_i = 5.0 \times 10^{-19} m^2$  the ion-neutral cross section in weakly ionized plasmas [31] and  $n_{neu}$  the total neutral density.  $\alpha$  is a free-parameter for magnetic multi-cusp confinement effect on loss area ( $\alpha=0.33$ )[30]. Therefore, in the equations, unknown values are n<sub>H</sub>, n<sub>H2</sub>, n<sub>1</sub>, n<sub>2</sub>, n<sub>3</sub>, T<sub>e</sub>, the given values are V/A<sub>eff</sub>, v<sub>0</sub>, T<sub>g</sub> and  $\gamma$ . Not only ion species ratios but also electron temperature can be obtained with a variation of plasma parameters of electron density, gas pressure and chamber geometry.

## 2.2 Calculation of electron temperature of the hydrogen plasma

As expected from the chapter 1. 3., the result of particle balance shows T<sub>e</sub> does not depends on electron density, but the T<sub>e</sub> is determined given neutral gas density (n<sub>g</sub>) and effective plasma sizes (d<sub>eff</sub>= V/A<sub>eff</sub>). Consequently, T<sub>e</sub> is plotted by n<sub>g</sub> · d<sub>eff</sub> as shown in Fig. 2. 3. This result indicates that T<sub>e</sub> of hydrogen plasma increase with

decreasing operating pressure and  $d_{\text{eff}}$ . In considering geometry of TCP based H-ion source, It is a cylinder of radius  $R = 10$  cm and length  $L = 11.5$  cm.  $T_e$  is calculated about 9eV with 3mTorr operating pressure in which minimum operating regime of the ion source for the stability. From this result it can be also expected that more increase  $T_e$  can be obtained with smaller  $d_{\text{eff}}$  value in the same operating pressure. To realize reduce of the  $d_{\text{eff}}$  value, change of discharge chamber length is a practical approach in this configuration to increase  $T_e$ . Therefore, higher  $T_e$  which is basically required to generate higher vibrationally excited molecules in volume H- production is also achievable with reducing chamber length besides decreasing operating pressure.

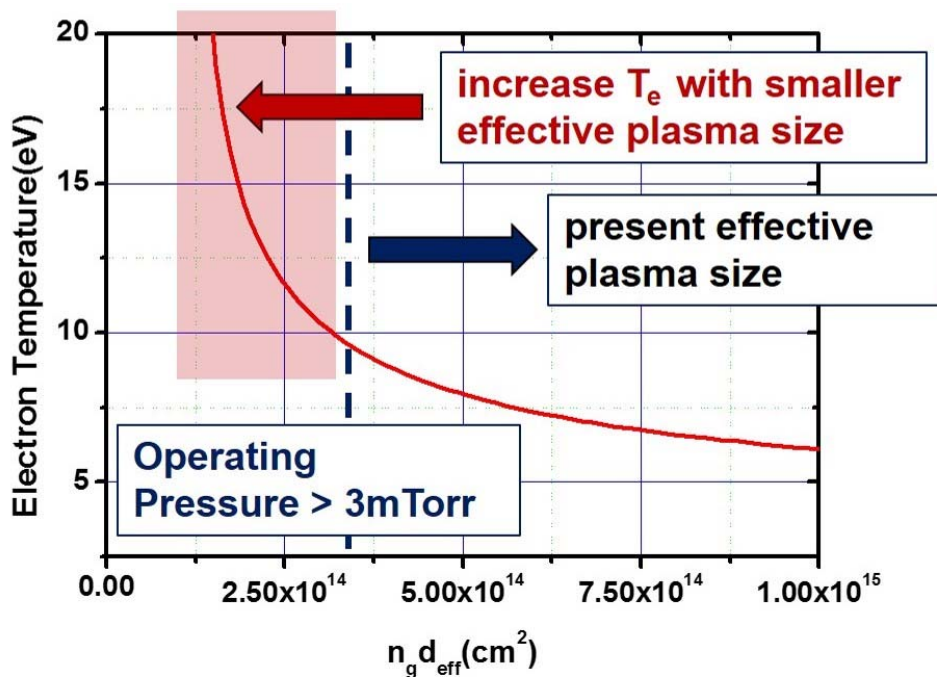


Figure 2.3 Calculated electron temperature of hydrogen plasma for various effective plasma size and neutral gas density.

## Chapter 3 Effects of chamber configuration on plasma parameters and H<sup>-</sup> ion production

### 3.1 Experimental setup

#### 3.1.1 Discharge chamber configuration

A cylindrical discharge chamber without H<sup>-</sup> ion beam extraction system has been newly designed to accommodate several vacuum ports for diagnostics of plasma properties. The new chamber has the identical geometry to the TCP based H<sup>-</sup> ion source and the magnetic structure is also designed to be the same as. [27] According to the characteristics of T<sub>e</sub> from the particle balance calculation for various d<sub>eff</sub> values in chapter 2, two discharge chambers with different lengths are used to investigate the change of electron temperature for the different d<sub>eff</sub>. It is

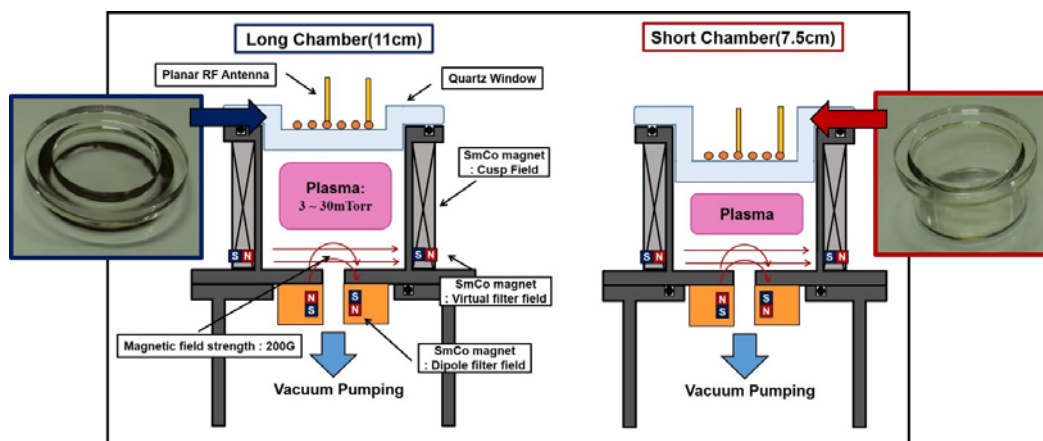


**Figure 3.1 Two discharge chambers with different lengths to investigate the change of plasma parameters for the different effective plasma size.**

noted that shortening the chamber length means reduction of the effective plasma size, thus increase of the electron temperature. The length of the discharge chamber can be easily varied by changing the depth in recess of the quartz plate located at the top of the discharge chamber. Two different chambers with length of 7.5 cm (referred as ‘short chamber’) and 11 cm (referred as ‘long chamber’) are obtained by using two quartz plates with different recess depth. Note that the discharge chamber of 11 cm in length is identical to that previously used for ion beam extraction.[27] A schematic diagram of the chamber configuration with different lengths is depicted in Fig. 3. 1. Radio-frequency (rf) power with driving frequency of 13.56 Mhz is delivered to a loop antenna located on the quartz plate. Simultaneous diagnostics of plasma properties have been carried out with rf-compensated cylindrical Langmuir probes in two different regions, i.e. the driving region and the extraction region as shown in Fi. 3. 2. One is located at the position 2 cm below the quartz plate and the other is located at 1 cm above the plasma electrode. In addition, a laser photo-detachment technique with an Nd-YAG laser of 532 nm in wavelength has been utilized to measure the  $H^-$  ion density in the extraction region.

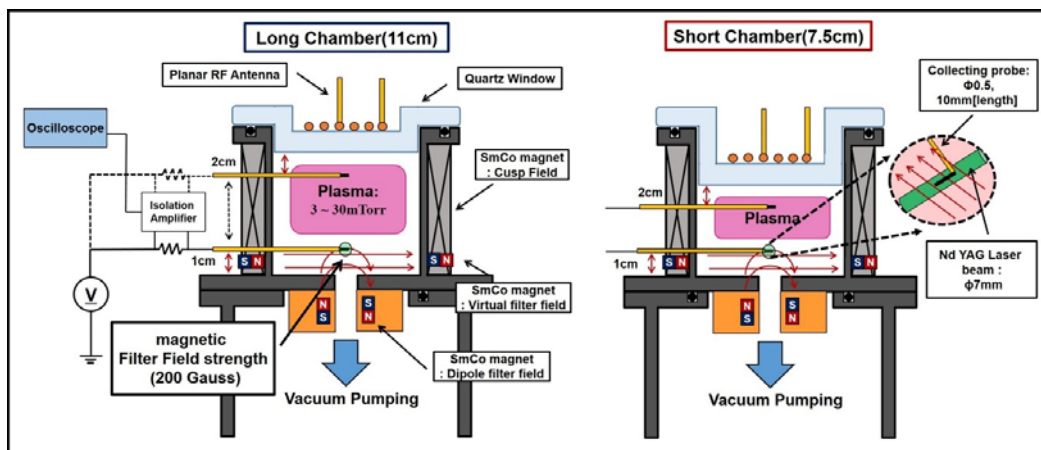


**Figure 3.2 Langmuir probe and laser photo-detachment diagnostic system to measure plasma parameters.**

### 3.1.2 Langmuir probe diagnostic

The Langmuir probe would be the most popular tool to diagnose low temperature plasmas because of its simplicity and high spatial resolution [29]. What we have to do is to place a small conducting tip in plasma and measure currents as varying voltages on it, as shown in Figure 3.3 (a). From the correlation between the measured current and voltage, plasma properties can be analyzed. Single tip Langmuir probe, most widely used among the probes, gives basic properties of plasmas such as plasma density, electron temperature, plasma potential and floating potential (Figure 3.3 (b)-(d)), and electron energy distribution function.

#### ➤ Basic analysis of Langmuir probe data

Basic analysis of probe data is useful if the following two assumptions are satisfied: 1) the sheath surrounding the probe is collisionless, 2) surface area of the sheath is almost same with the physical area of the probe  $A_{LP}$  when sheath thickness around the probe tip  $s$  is quite thin, compared to the probe area ( $A_{LP} \gg s^2$ ) [29]. A typical current-voltage (I-V) curve from single Langmuir probes is depicted in Figure 3.3 (b). There are five distinguished regions named as ion saturation region, floating potential, electron retarding region, plasma potential and electron saturation region (which are described in some references in detail [29, 32-34]), respectively. Among them, plasma potential  $V_p$  indicates the voltage at the knee of the I-V curve. More precisely, the plasma potential can be determined as the voltage in which the first derivative of the I-V curve,  $dI_{LP}/dV_{LP}$  is maximized (Figure 3.3 (c)). Also, the voltage at the cross point between linear lines extrapolated from electron saturation region and electron retarding region in semi-log plot of I-V curve (Figure 3.3 (d)) indicates the plasma potential.

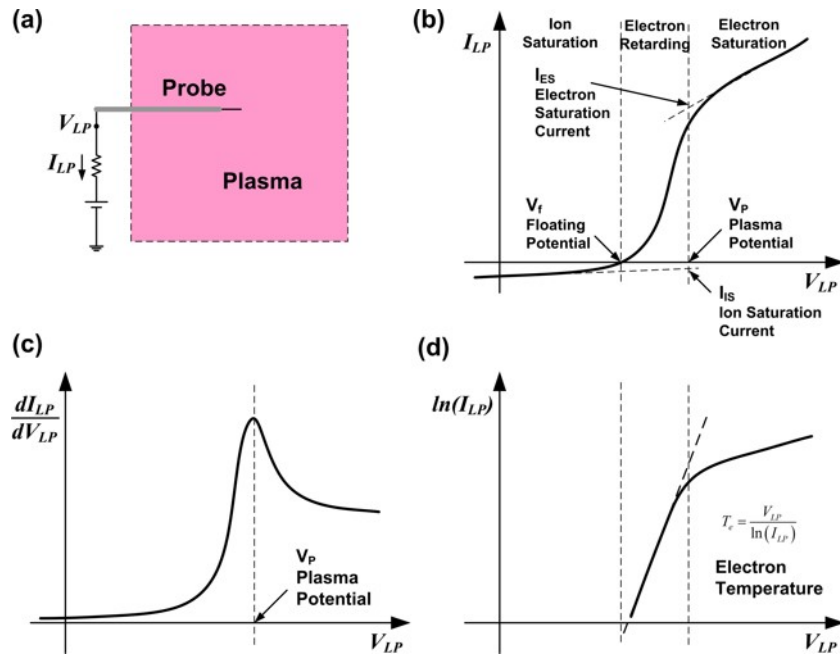


**Figure 3.3 (a) Schematic diagram of Langmuir probe and circuitry, (b) a typical current-voltage (I-V) curve of Langmuir probe, (c) 1<sup>st</sup> derivative of the I-V curve and determination of plasma potential, and (d) semi-log plot of the I-V curve and linear fit to find electron temperature.**

Electron temperature,  $T_e$ , is estimated from electron retarding region. If the distribution of electrons in plasmas follows Maxwellian distribution, the electron temperature is described as a function of the current and voltage of the probe. The electron temperature can be acquired by fitting I-V curve in the voltage range between the floating and plasma potential with the equation given by [29],

$$\ln\left(\frac{I_e}{I_{ES}}\right) = \frac{1}{T_e}(V_{LP} - V_p)$$

where  $I_e$  is electron current,  $I_{ES}$  electron saturation current, and  $V_{LP}$  probe voltage. Practically, the inverse value of the slope of the semi-log graphs indicates the

electron temperature, as depicted in Figure 3.3 (d). Floating potential,  $V_f$  means the voltages at which the net current is zero. Assuming that the ion current is described as Bohm current and electron current is one-directional thermal current from Maxwellian distribution, the difference between the plasma potential and the floating potential is a function of ion mass  $M_i$ , electron mass  $m_e$  and electron temperature  $T_e$  as following equation [29, 32-34].

$$V_p - V_f = T_e \ln \left( \frac{M_i}{2\pi m_e} \right)^{1/2} + \frac{T_e}{2}$$

In this manner, electron temperature can be deduced from the plasma and floating potentials, as well.

Plasma density  $n_e$  has a correlation with both the ion saturation current and electron saturation current as follows.

$$I_{ES} = \frac{1}{4} e n_e v_{eth} A_{LP}$$

$$I_{IS} = e n_s u_B A_{LP}$$

where  $v_{eth}$  is electron thermal velocity,  $I_{IS}$  ion saturation current,  $n_s$  plasma density at sheath edge, and  $u_B$  Bohm velocity.

As shown in the Eq. (2.3),  $I_{ES}$  is a function of plasma density  $n_e$ , electron velocity  $v_{eth}$  and probe area  $A_{LP}$ .  $I_{ES}$  can be determined as the linearly extrapolated value of the electron current in the electron saturation current region at plasma potential (Figure 3.3. (b)). Assuming the Maxwellian distribution, electron thermal velocity  $v_{eth}$  is described as a function of electron temperature as following,

$$v_{eth} = \left( \frac{8kT_e}{\pi m_e} \right)^{1/2}$$

where  $k$  is the Boltzmann's constant. Therefore, plasma density can be calculated if the electron saturation current and electron temperature are determined.

Langmuir probes are connected to the probe circuit through a RF choke of which impedance is over  $>100$  kohm for 13.56 MHz, in order to suppress unexpected RF noise. [33]

Based on this Langmuir probe diagnostic theory, electron temperature and density have been carried out with rf-compensated cylindrical Langmuir probes in two different regions, i.e. the driving region and the extraction region. One is located at the position 2 cm below the quartz plate and the other is located at 1 cm above the plasma electrode as shown in Fig. 3. 2. A tungsten wire with a radius of 0.15 mm and a length of 1.1 mm is used as a collecting tip of the cylindrical Langmuir probes.

### 3.1.3 Laser photo-detachment diagnostics

The laser photo-detachment diagnostic technique has been widely used for measuring  $H^-$  density in the hydrogen plasma.[35-39] This method is based on the interaction process between  $H^-$  ion and photons. A laser source which has a photon energy larger than the electron affinity of hydrogen is used to detach the electrons from  $H^-$  ions, and photo-detached electron current are collected by a Langmuir probe biased at a constant voltage above plasma potential. Before the laser pulse duration, the Langmuir probe draws a constant electron current  $I_{e0}$ , according to the electron density. Just after the laser pulse increase of current  $I_{e0}+\Delta I$  takes place which indicates increase of photo-detached electron density according to the  $H^-$  ion density, and the probe current remains nearly constant at  $I_{e0}+\Delta I$  for typically a few hundred nanoseconds. Fig. 3. 4. Shows that the typical photo-detachment signal of established result for measuring  $H^-$  ion density in prototype RF ion source for ITER NNBI and TCP based  $H^-$  ion source used in this experiment.

Consequently, the constant electron current  $I_{e0}$  prior to the laser pulse corresponds to the electron density and the increase in current  $\Delta I$  correlated with the negative ion density as following

$$\frac{\Delta I}{I_{e0}} = \frac{n_{H^-}}{n_e}$$

However, this indicates that several criteria have to be satisfied: (1) the laser pulse energy is sufficient to detach all the  $H^-$  ions in the irradiated volume, (2) the additional electrons are excluded due to other ways of detachment processes such as ionization of plasma particles or particles from ablation of material from the collecting probe, (3) the plateau is clearly identified, i.e. the radius of the laser irradiated volume is larger than the effective collection radius of the probe, (4) the probe bias voltage is well above the plasma potential to collect all detached electrons.

In order to assure the first criteria the fraction of detached ions can be calculated as function of the laser beam energy [35, 36]

$$\frac{\Delta n_{H^-}}{n_{H^-}} = 1 - \exp\left(-\frac{\sigma E}{h\nu A}\right)$$

with  $\sigma$  being the photo detachment cross section,  $h\nu$  the photon energy and  $E/A$  the laser beam energy density. Since the electron affinity of negative hydrogen ions is 0.745 eV [35, 36], the second harmonics of a Nd :YAG laser ( $\lambda = 532$  nm,) which corresponds to an energy of 1.16 eV, is used for the photo detachment due to the advantage of allowing easier alignment of the experimental setup. The detachment cross section at this frequency is  $\sigma = 3.0 \times 10^{-21} \text{ m}^2$ . [39] Therefore, 99% of the negative ions can be destroyed with a laser beam energy density of  $80 \text{ mJ/cm}^{-2}$ . As shown in Fig. 3. 5, detaching current is saturated depending on the increase of laser energy density and this experimental result is quite well matched

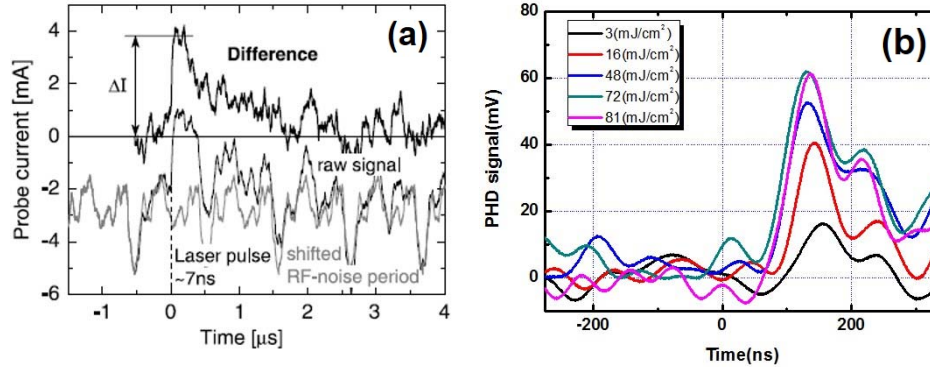


**Figure 3.4 Comparison of measured laser photo detachment diagnostic signal in (a) prototype RF ion source for ITER NNBI [36] and (b) TCP based H<sup>-</sup> ion source.**

to the calculated fraction of detached ions for the laser energy. This wavelength fulfils also criteria (2), namely that the photon energy is relatively low to interact with other plasma particles as hydrogen particles.[38,39] Criteria (3), the requirement to have a laser irradiated volume larger than the effective collection radius of the probe, is satisfied by using a laser irradiated volume of 10mm in diameter and a probe tip of 0.3 mm in diameter. The radius for the probe collection area is estimated to be smaller than 8mm. Criteria (4), that the probe voltage is high enough to collect all detached electrons, is verified by performing a scan in the applied probe voltage as shown in Fig. 3. 6. The signal reaches a saturation region and a probe voltage of typically 30V is applied above the plasma potential in all the measurements. Based on this laser photo-detachment diagnostic method, H<sup>-</sup> ion density have been carried out in extraction regions located at 1 cm above the plasma electrode as shown in Fig. 3. 2.

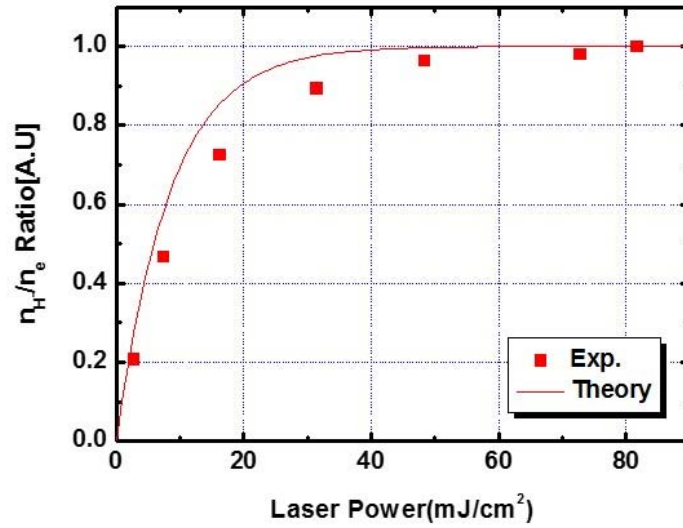


Figure 3.5 Saturation of LPD signal for laser power density.

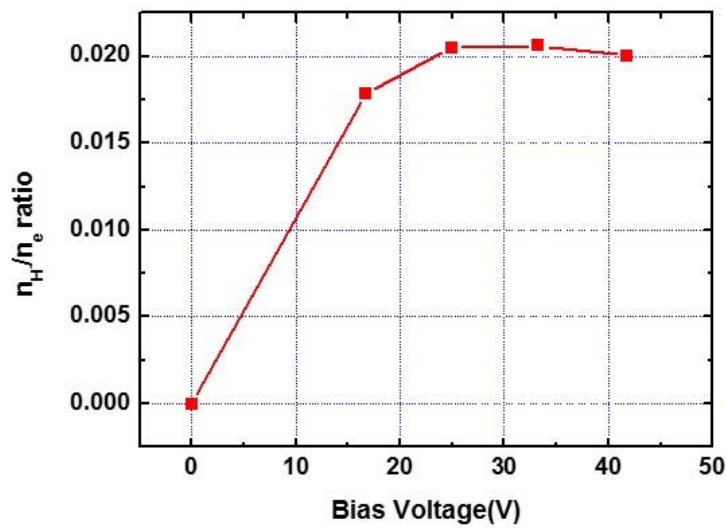


Figure 3.6 Validation of  $n_H/n_e$  ratio for various probe bias voltage.

## 3.2 Effects of various chamber lengths on characteristics of plasma parameters and H<sup>-</sup> ion production

### 3.2.1 Characteristics of plasma parameters for change of chamber length

As describe in chapter 1, increasing production of highly vibrationally excited molecules are firstly required to generate H<sup>-</sup> ion effectively in volume produced negative H<sup>-</sup> ion source. Therefore higher electron temperature and density in driver region should be established. Fig. 3. 3(a). shows the variation of the electron temperature and density in the driver region with various rf power and gas pressure for two different chamber lengths. As expected from results of the particle balance model described in chapter 2, it is clearly observed that the electron temperature is greatly influenced by the length of the discharge chamber as well as the operating gas pressure. Almost 50% increase in the electron temperature is achieved by shortening the chamber length from 11 cm to 7.5 cm (30% reduction) at the same operating pressure. More surprisingly, the electron temperature is almost not changed by rf power, which indicate electron temperature is hardly depends on electron density as shown in Fig. 3. 7. In addition, the electron temperatures calculated using the particle balance model show fairly good agreements with the experimental results as shown in Fig. 3. 8., despite the simulation tends to overestimate the electron temperature at low pressure regime. Operation at low pressure regime would make the electron energy distribution non-Maxwellian, invalidating the assumption used in the simple model. Accordingly, in our experimental conditions, it is proven that the electron temperature in the heating region can be easily increased by reducing the chamber length at given operating pressure.

As expected from previous results, the electron density increases with rf power and gas pressure in both chamber configurations. However, in comparing electron

density between the both configurations as shown in Fig. 3. 9., relatively lower electron density is obtained in the operating pressure below ~10 mTorr with the short chamber length configuration, but as increasing operating pressure, higher electron density is obtained above the pressure, this result can be explained by a simple power balance equation as follows [29]

$$n_e \propto \frac{1}{u_B(\sqrt{T_e})A_{eff}(Loss\ Area)\epsilon_T(T_e)}$$

where  $n_e$  is electron density,  $u_B$  Bohm velocity,  $A_{eff}$  effective loss area,  $\epsilon_T$  total ionization rate. From this equation, electron density is proportional to the inversed electron temperature & loss area value at the same absorbed RF power. Therefore electron density more decrease with short chamber length due to higher electron temperature but decrease of electron density can be compensated by reducing loss area.

Consequently, characteristics of plasma parameters from this experiment indicate that not only electron density can be controlled by RF power, and loss area, but electron temperature is also controllable with various effective plasma size for a given operating pressure of the  $H^-$  ion source, which are essential to generate highly vibrationally excited molecules for higher volume  $H^-$  production.

Based on the plasma parameters in heating region, the electron density and temperature measured in the extraction region is shown in Fig. 3. 4. Their dependencies on the gas pressure, rf power and chamber length are almost the same as those measured in the heating region. However, due to the magnetic filter field of ~200 Gauss, the electron density and temperature are greatly reduced in the extraction region. Experiments show that the ratio of the electron temperature in the heating region and the extraction region is almost constant at given magnetic filter strength. Therefore, higher magnetic field strength is required for the short chamber to reduce the electron temperature down to the level of the longer one.

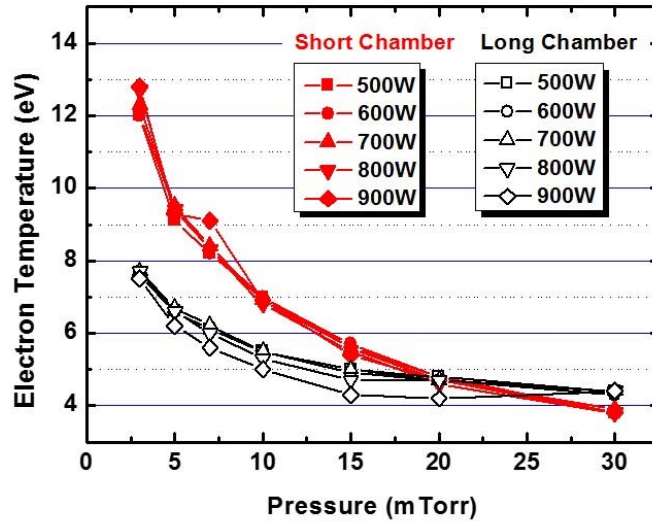


Figure 3.7 Measured electron temperature with various input RF power for change of chamber length.

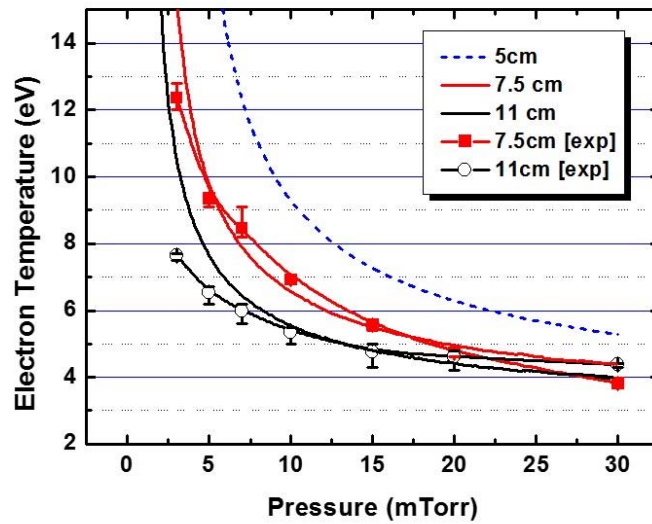


Figure 3.8 Measured electron temperature and comparison with the results of particle balance model.

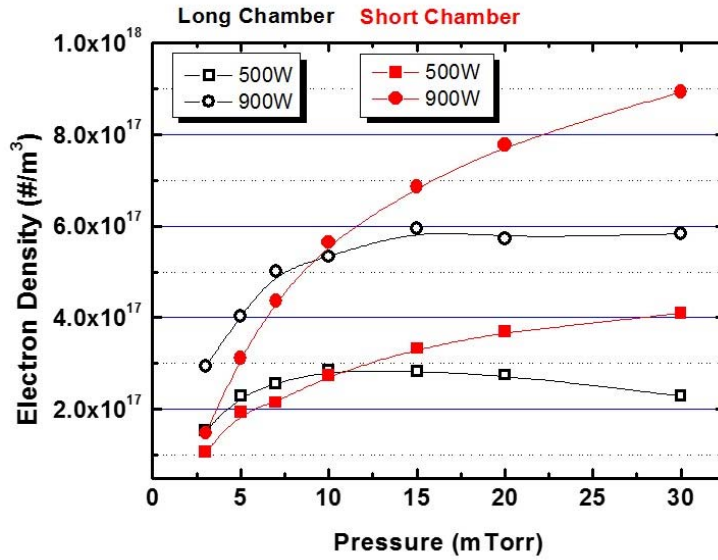


Figure 3.9 Electron density with various operating pressure and input RF power for change of chamber length.

### 3.2.2 H<sup>-</sup> ion production for various plasma parameters

Direct measurements of H<sup>-</sup> ion density in the extraction region with a laser photo-detachment technique clearly show the effects of the discharge chamber length on the production of negative ions. As depicted in Fig. 4, overall H<sup>-</sup> ion density is observed to increase with the reduction of the chamber length and the increase of rf power. The increase of H<sup>-</sup> ion density with rf power is quite natural because the electron density increases monotonically with rf power without change in the electron temperature, as shown in Figs. 3. 10.

Significant change in H<sup>-</sup> ion density with gas pressure for both long and short chambers can also be explained from the probe data quite clearly. For the operating pressure over around 7 mTorr, the H<sup>-</sup> ion density of the short chamber is much higher than that of longer one. This is because the electron temperature is still higher enough to generate vibrationally-excited molecules. However, further increase of the gas pressure up to ~15 mTorr makes the electron temperature too low to generate vibrationally-excited molecules, thus reducing H<sup>-</sup> ion density in the extraction region. On the other hand, the reduction of gas pressure below the optimum value of ~15 mTorr results in too high electron temperature in the extraction region such that the generation of H<sup>-</sup> ions by dissociative attachment is reduced and electron stripping loss is also enhanced there. The shift of the optimum pressure to a lower value of ~7 mTorr for the long chamber strongly supports this explanation. In our experimental conditions, the H<sup>-</sup> ion density seems to be generated optimally at the electron temperatures of 0.5 eV in the extraction region, irrespective of the chamber length. This result is believed to be due to too high electron temperature in extraction region along with heating region. In other word, high-energy electrons increased in the extraction region deteriorate H<sup>-</sup> ion production by reducing dissociative attachment with vibrationally-excited hydrogen molecules or destroying H<sup>-</sup> ions. Therefore, lowering the electron

temperature in the extraction region is required to enhance the H<sup>-</sup> ion production in extraction region furthermore even at low operating pressure.

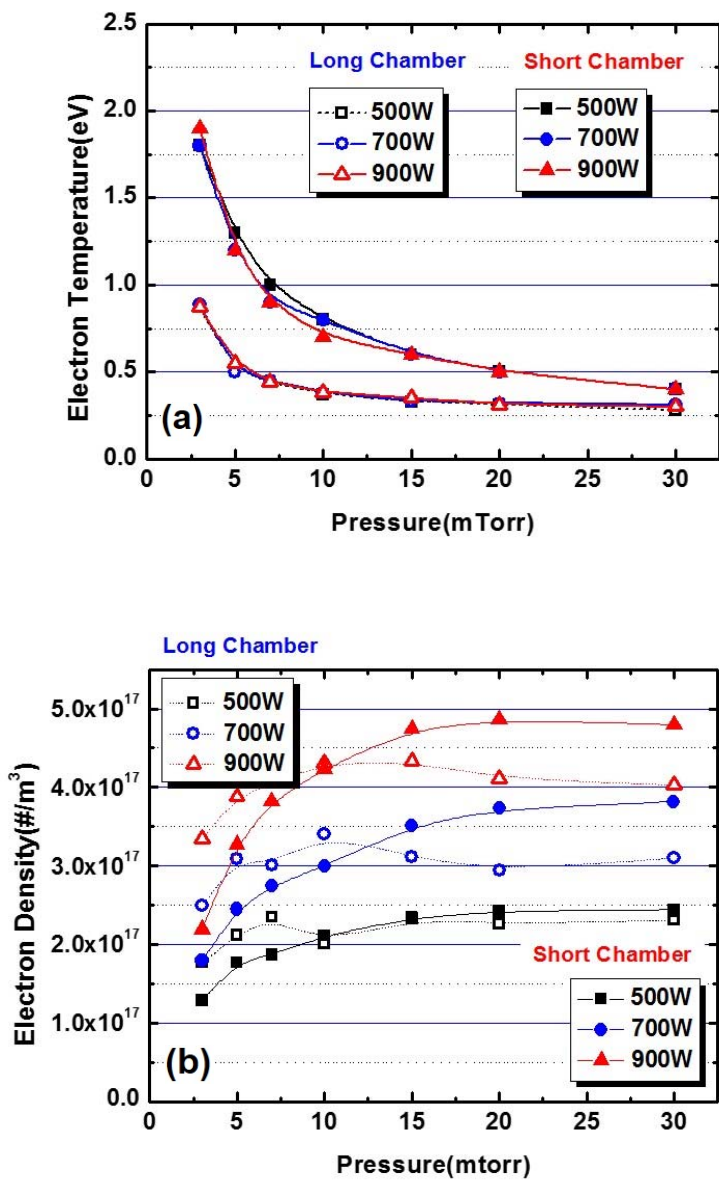


Figure 3.10 Measured electron (a) temperature and (b) density in the H-extraction region with various input RF power for change of chamber length.

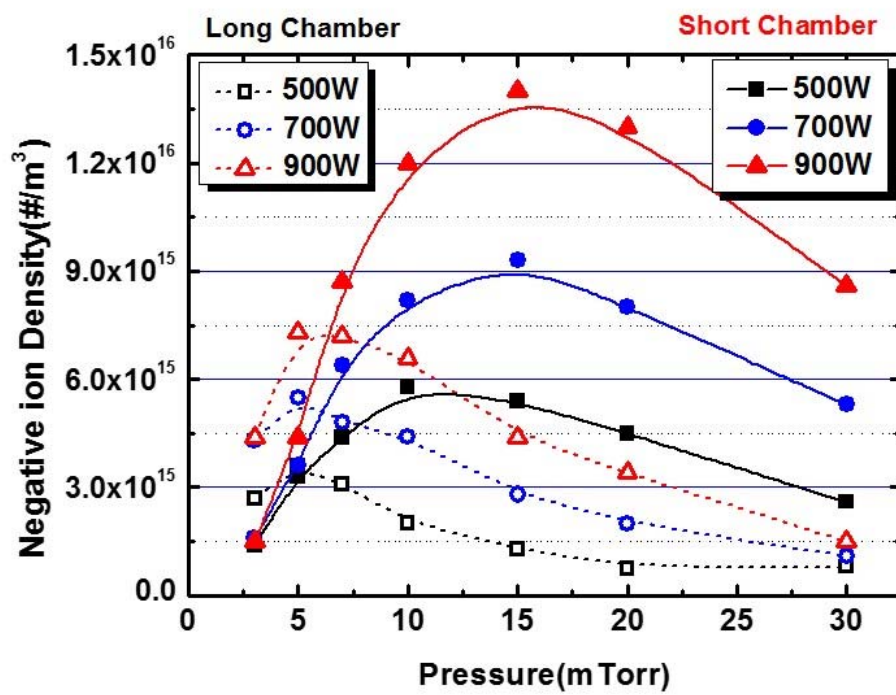


Figure 3.11 Characteristics of measured H- ion density with various pressure and input RF power for change of chamber length.

### 3.3 Effects of various magnetic filter field on characteristics of plasma parameters and H- ion production

#### 3.3.1 Characteristics of plasma parameters for change of magnetic filter field

As the chamber length significantly affects the electron temperature at the heating region, it is important to filter out the high energy electron for the effective control of the electron temperature at the extraction region and consequent enhancement of H- ion production. The filter magnetic field is commonly used for the lower the electron temperature at the extraction region, but the effect of filter magnetic field on the plasma parameters is not well understood. In order to investigate the effect of the filter magnetic field on the electron temperature, plasma parameters have been measured under various number of magnets that generate transverse filter magnetic field.

Figure 3. 12. shows the measured  $T_e$ ,  $n_e$ ,  $n_{H^-}$  with various filter magnetic field strength of 140, 170 and 200 Gauss under two different chamber length. Due to

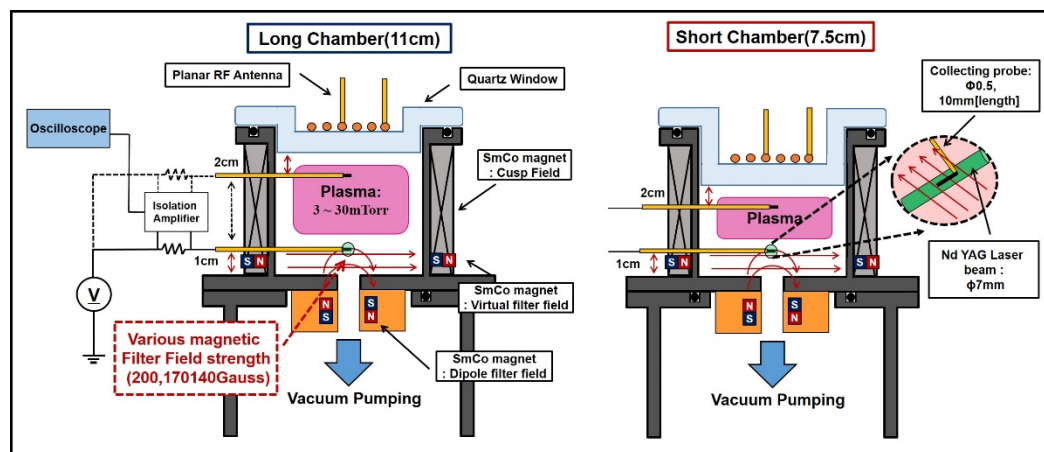


**Figure 3.12 Measurement of negative ion density for various magnetic filter field configurations.**

the structure of the vacuum chamber, it is not possible to increase the filter magnetic field over 200 Gauss. Figure 3. 13(b). shows that the electron temperature at the extraction region decreases as the filter magnetic field strength increase. Note that the increase of filter magnetic field can cause the overestimation of the electron temperature, therefore the actual temperature with strong filter magnetic field can be lower. Note that under identical filter magnetic field strength, the electron temperature under short chamber length is 50 % larger than that under long chamber length. Note that the plasma parameters at the heating region are almost independent to the filter magnetic field strength even with highest filter magnetic field strength. Thus the filter field strength at the extraction region does not affect the production of vibrationally- excited molecules. As shown Fig 3. 13, the electron temperature at the extraction region varies significantly as the filter magnetic field varies but the electron temperature at the extraction region remains almost unchanged with varying magnetic field strength, which varies less than 20%.

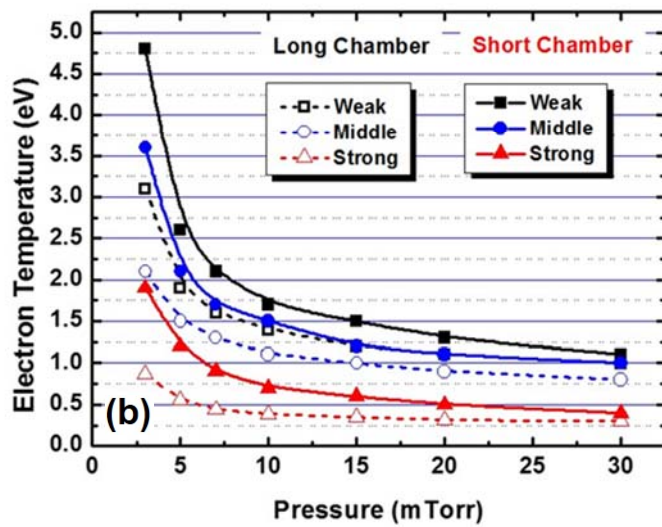
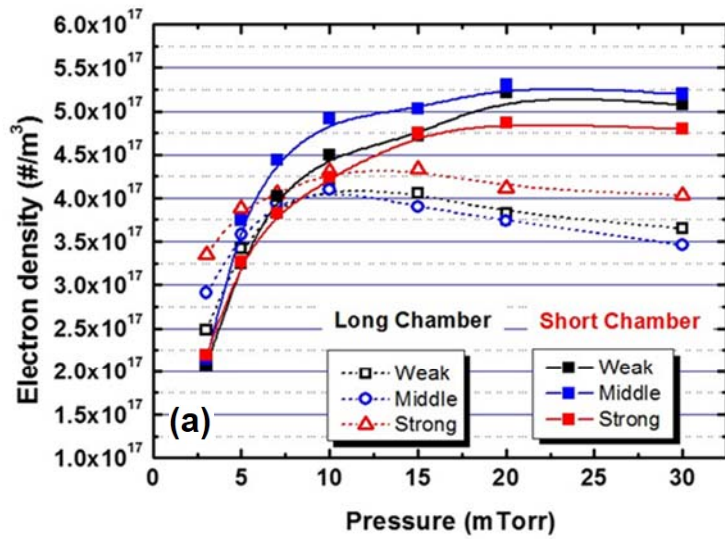


Figure 3.13 Measured electron (a) density and (b) temperature with various magnetic filter field strengths for change of chamber length.

### 3.3.2 H<sup>-</sup> ion production for change of magnetic filter field strength

The H<sup>-</sup> density has been measured with various filter magnetic field strength under two different chamber length based the plasma parameters measured at the identical condition. Figure 3. 14. shows the measured H<sup>-</sup> density under two RF power of 500 and 900W, two different chamber length, various filter magnetic field strength and various operating pressure. The H<sup>-</sup> density under short chamber length is much higher than that under long chamber with identical magnetic filter strength when operating pressure is sufficiently high. The maximum H<sup>-</sup> density under short chamber length is almost 10 times larger than that under long chamber length with identical filter magnetic field strength. Note that H<sup>-</sup> density increases as filter magnetic strength increases under both RF used and both chamber length. To investigate the influence of filter magnetic field strength on the H<sup>-</sup> density, rate of change of electron temperature and density at the extraction region with varying operating pressure has been compared with the rate of change of H<sup>-</sup> density at the extraction region with varying operating pressure under various filter magnetic field strength. The increase rate of H<sup>-</sup> density as a function of operating pressure is higher at the low operating pressure and increases as the strength of filter magnetic field increases. Figure 3. 16. shows the increase rate of electron density as a function of operating pressure remains rather constant as the operating pressure and filter magnetic field strength changes. However, as shown in Figure 3. 15, the electron temperature significantly decreases as operating pressure increases or filter magnetic field strength increases. Even under different chamber length condition, when the electron temperature is similar then the increase rate of H<sup>-</sup> density is similar. Therefore the increase rate of H<sup>-</sup> density is closed related with the electron temperature at the extraction region. This result can be explained as following. Under short chamber length, the electron temperature at the heating region increases and the production of highly vibrationally-excited molecules

increases. Therefore when the electron temperature sufficiently low by filter magnetic field and consequently the stripping loss by electrons is reduced and the production of H- density by DA process, the H- density under short chamber length is greater than that under long chamber length. Under similar electron temperature and density at the heating region, as the filter magnetic filter field gets stronger and consequently the electron temperature decreases, the peak H- density occurs at the lower operating pressure. Therefore under short chamber length, it is possible to increase the H- density by using higher filter magnetic field strength at the low operating pressure which is required for practical use of H- ion source as the electron density does not change much but electron temperature will controlled effectively.

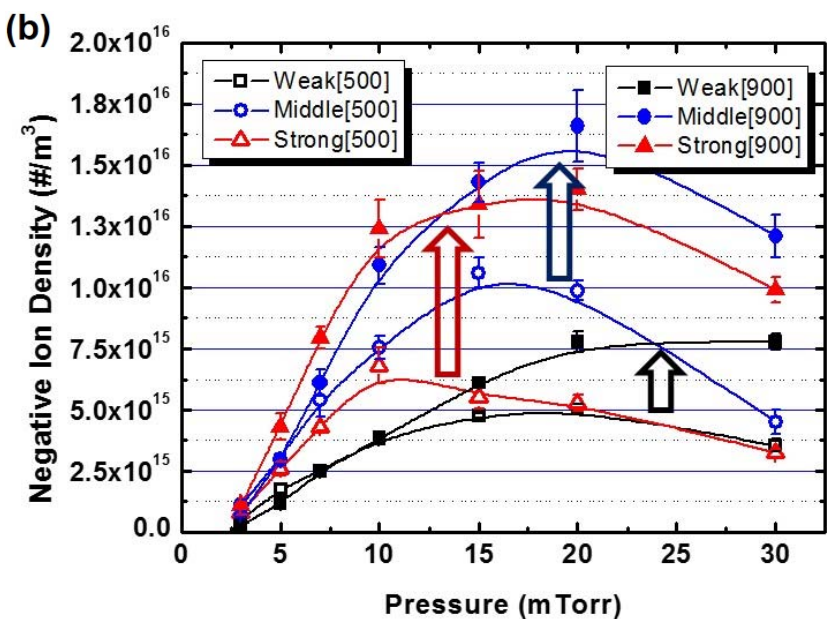
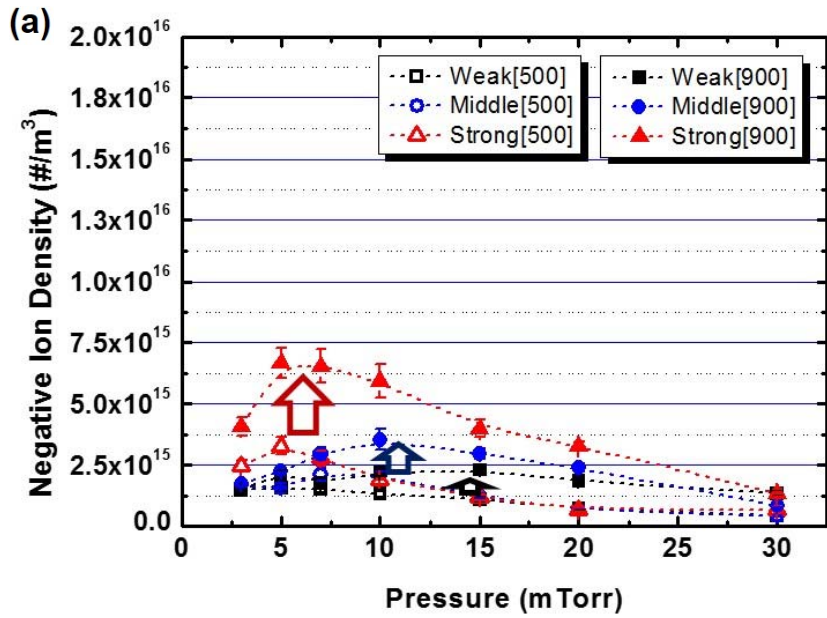


Figure 3.14 Measured H- ion density for various magnetic filter field configurations in (a) long and (b) short chamber length configurations.

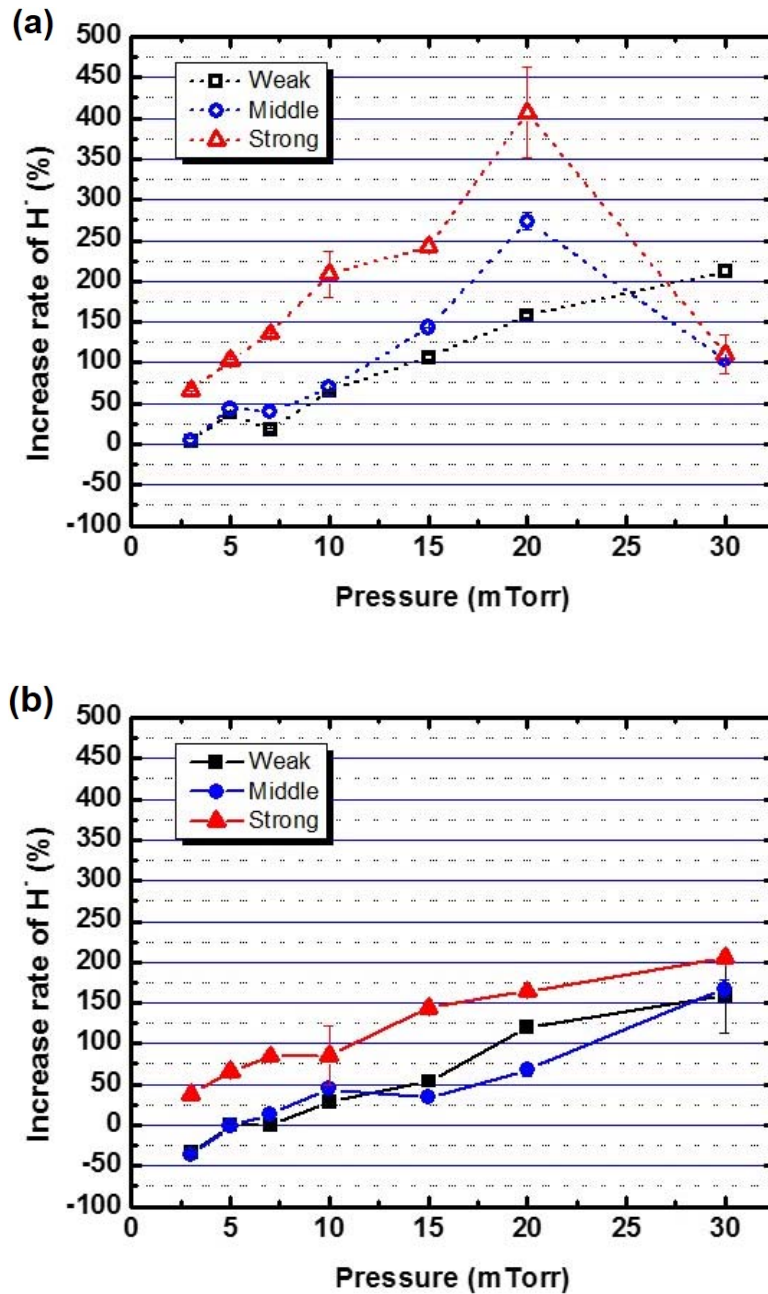


Figure 3.15 Increasing rate of H<sup>+</sup> ion density for various filter magnetic field strengths with the same increased RF input power in (a) long and (b) short chamber length configuration.

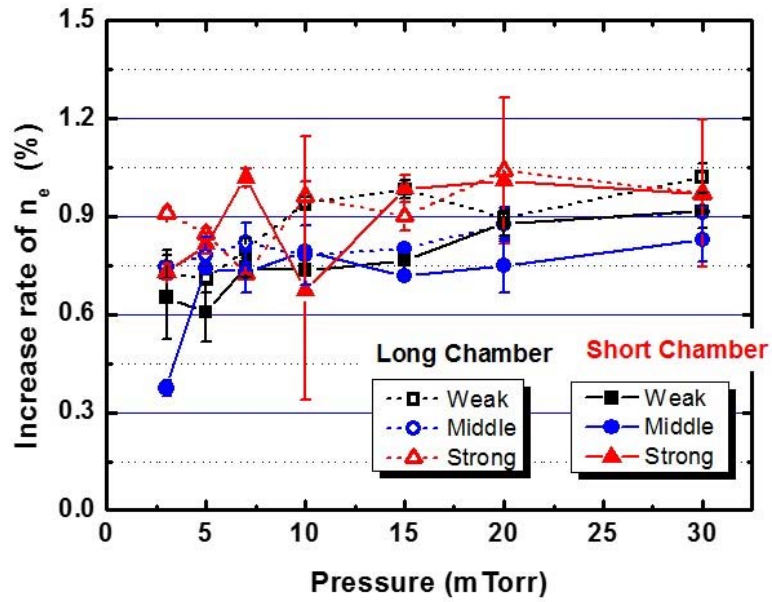


Figure 3.16 Increasing rate of electron density for various filter magnetic configuration with the same increased RF input power

## **Chapter 4 Extraction of negative ion beam current and analysis on $H^-$ ion transport in the volume-produced $H^-$ ion source**

### 4.1 Experimental setup

TCP based  $H^-$  ion source at SNU has a cylindrical configuration with inner diameter of 10cm and the length of 11cm. Radial structure of this source is made of stain-less steel, and 14 poles multi-cusp magnets are installed to enhance the confinement of the generated hydrogen plasma. The RF wave of 13.56Mhz with two-and-half-turn planar RF antenna was used to generate plasma. A background pressure of  $< 10^{-6}$  Torr is established, and a hydrogen pressure above 3mTorr is used in the source region with stability.

Reducing electron temperature in extraction region is highly required to enhance the volume production process of negative ion and suppress the destruction process due to increasing reactions with higher electron energy. To realize lower electron temperature in the extraction region, external magnetic filter field is used in the TCP based RF  $H^-$  ion source.[27] A pair of filter magnets called as virtual filter is installed in front of the extraction electrode to reduce the fast electrons. In addition to the virtual filter magnet, a set of dipole magnets is installed in the extraction electrode to enhance the magnetic filter field strength and to deflect co-extracted electrons. Measured magnetic field strength is 240G in front of extraction hole.

#### 4.1.1 H- ion beam extraction system

As shown in Fig. 4.1, a triode extraction system is used for negative ion beam extraction in the TCP negative ion source. Diameter of 8mm is the extraction aperture size and gap distance is 3.5mm between the plasma and the extraction electrode. An extraction voltage of  $V_{ex}=2\sim 4\text{kV}$  is applied between the plasma and the extraction electrode. A second voltage of  $V_{accel.}=0\sim 20\text{kV}$  is used to focus negative ion beam onto a faraday cup, which measure the negative ion current. Faraday cup is installed at the end of the beam transport region. Distance between acceleration electrode and faraday cup aperture is 30cm.

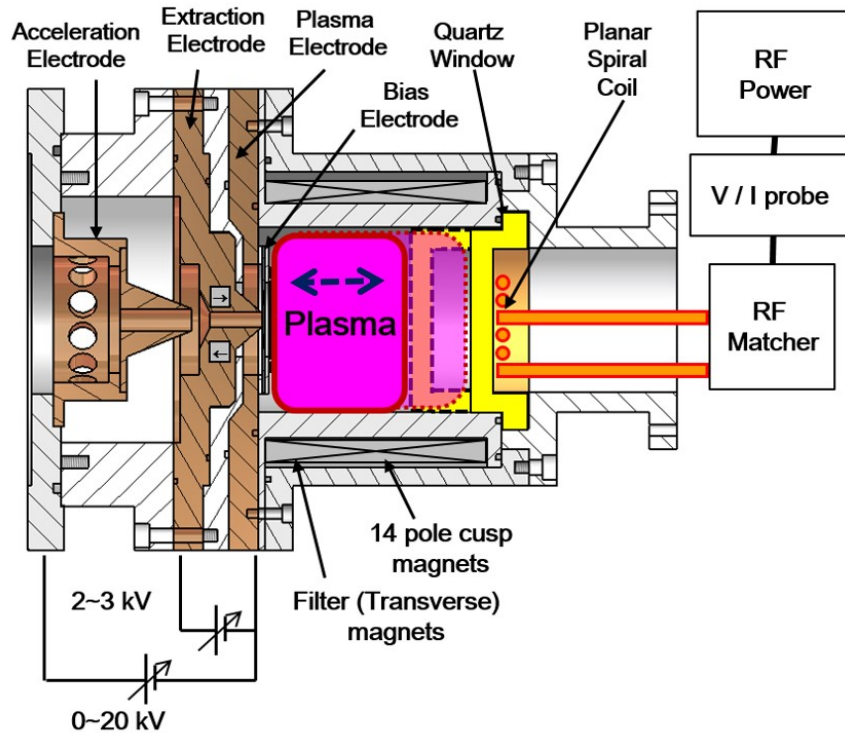
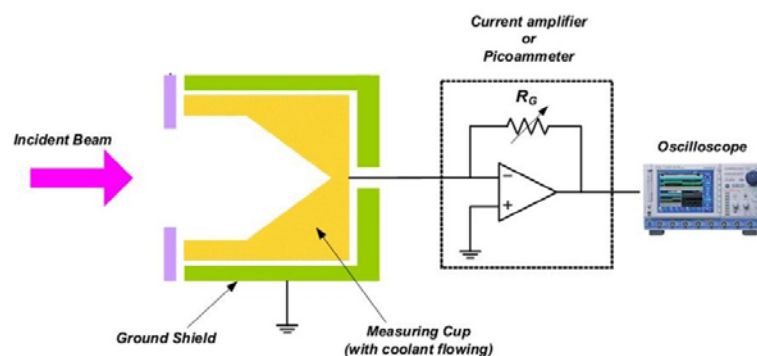


Figure 4.1 Drawing of TCP H- ion source with change of effective plasma size.

#### 4.1.2 Measurement of H<sup>-</sup> ion beam: Faraday cup

A Faraday cup is widely used to measure beam current at ion sources, due to the advantage of its simple structure, fast reaction and high accuracy. As shown in Fig. 4. 2, the extracted ion beam is incident on the electronically insulated cup and current resulted from the ion beam pass through the measuring resistor to the ground. The beam current is calculated from the voltage drop across the measuring resistor. The measurement accuracy by a Faraday cup is affected by a series of secondary processes created by beam impacting onto the cup (the emission of secondary electron and secondary ions, reflection of charged particles, etc.), the collection of electrons near the cup, current leakage to ground, and the penetration of the measured particles through the cup, etc. however, in most cases, the effect of the secondary electron emission is predominant for the coefficient of secondary ion emissions which is less than 2% to an order of magnitude for ion energy higher than 10 keV. When the secondary electrons escape from the collector, H<sup>-</sup> current will be underestimated.

The electron suppression electrode is commonly used to prevent the secondary electrons from entering or escaping the collector. Also, a magnetic field parallel to



**Figure 4.2 A schematic drawing of the Faraday cup.**

the surface target is used to retain secondary electrons. A long Faraday cup or a cone-shaped faraday cup is also efficient for capturing the secondary electrons. [38] The faraday cup used for this study has 20cm length and used permanent magnet to suppress secondary electron effect. The strength of magnet was chosen not to affect the trajectory of the H<sup>-</sup> ion beam.

## 4.2 Characteristics of H<sup>-</sup> ion beam current for change of chamber length

As shown in Fig. 4. 3, experiments with the reduced chamber length show a few times enhancement of H<sup>-</sup> ion beam currents compared to those extracted from the previous chamber design at operating pressures above 10 mTorr, which is consistent with the results expected from the increased H<sup>-</sup> ion populations. Compared to the maximum H<sup>-</sup> ion beam current of 1.15 mA (3.3 mA/cm<sup>2</sup>/kW) measured at operating pressure of 5 mTorr for the long chamber, the maximum H<sup>-</sup> ion beam current of 1.55 mA increased by about 40% is achieved with the short chamber at operating pressure of 7 mTorr, which is comparable to the highest H<sup>-</sup> current density per unit RF power of the established major volume-produced H<sup>-</sup> ion sources. In addition, it is clearly observed that the optimum operating pressure for obtaining the maximum H<sup>-</sup> ion beam current shifts to high pressure regime by shortening the discharge chamber length. This result is believed to be due to too high electron temperature in extraction region along with heating region in the case of the short chamber, as discussed previously. In other word, high-energy electrons increased in the extraction region deteriorate H<sup>-</sup> ion production by reducing dissociative attachment with vibrationally-excited hydrogen molecules or destroying H<sup>-</sup> ions. Therefore, lowering the electron temperature in the extraction region is required to enhance the H<sup>-</sup> ion beam current furthermore even at low operating pressure with the short chamber. Nevertheless, a few times

enhancement of H<sup>-</sup> ion beam current by reducing the discharge chamber length achieved in the experiment with RF-driven TCP ion source is quite impressive in terms that it is achieved only by changing chamber geometry without providing additional heating power.

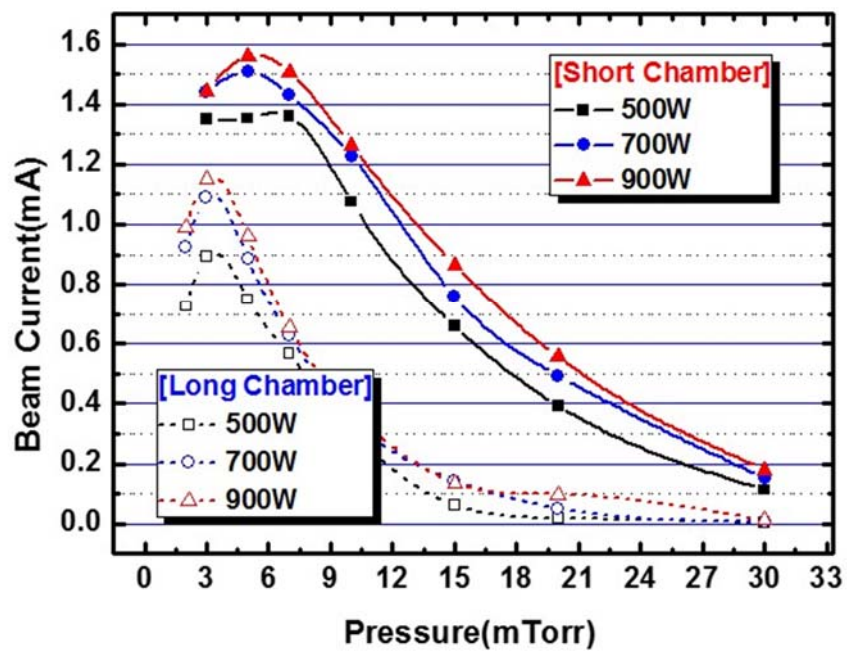


Figure 4.3 Extracted H- ion beam current for different effective plasma size with various operating pressure and RF power.

### 4.3 Analysis of correlation between extracted H<sup>-</sup> ion beam current and measured H<sup>-</sup> ion density

As shown in Fig. 4.3, it is worth noting that even though measured H<sup>-</sup> ion density decrease in the low operating pressure regime with the short chamber due to higher electron temperature in the extraction region, higher H<sup>-</sup> ion beam current is obtained in the low operating pressure regime from the beam extraction result. Therefore, this discrepancy is analyzed in considering of neutralization of H<sup>-</sup> ion beam in the transport region and additional reaction processes between the measuring position and the extraction hole region.

#### 4.3.1 Neutralization of H<sup>-</sup> ion in the beam transport region

The extracted H<sup>-</sup> ion beam can be reduced by neutralization with hydrogen molecules when it passes through the beam transport region. In order to calculate the loss of H<sup>-</sup> beam by neutralization, the pressure between the extraction and acceleration region has been estimated to be a half value by assuming that the pressure decreases linearly between measured operating pressure of the ion source

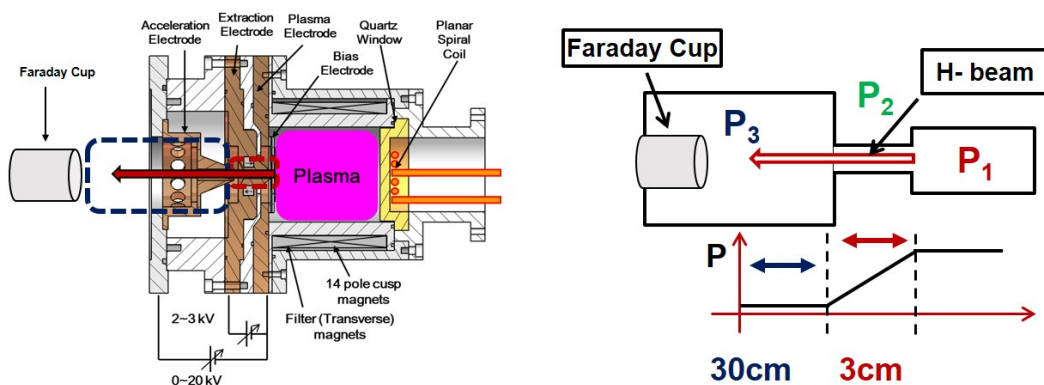


Figure 4.4 Estimation of residual gas pressure in the H<sup>-</sup> ion beam transport.

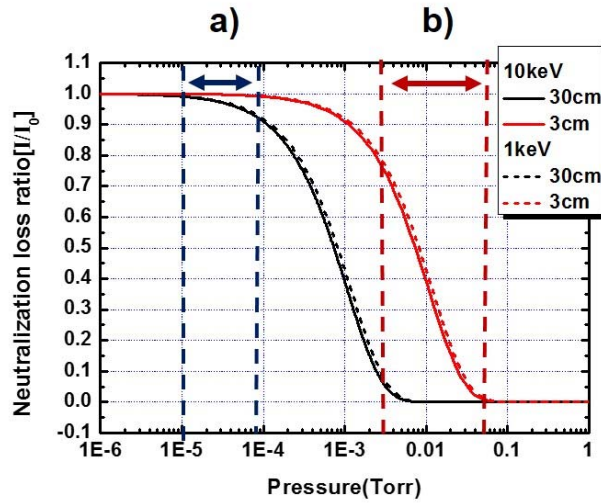


Figure 4.5 Neutralization loss ratio for various background gas pressure.

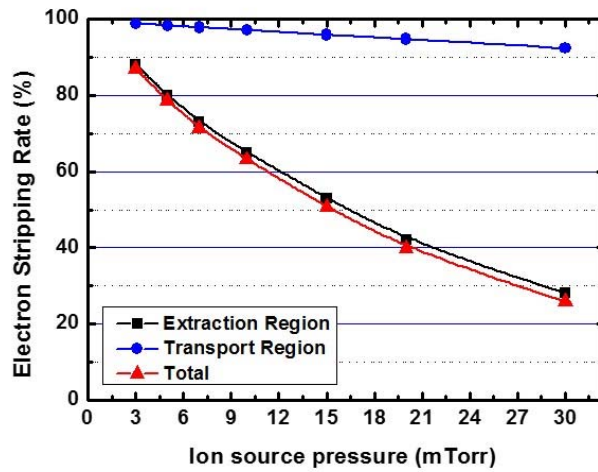


Figure 4.6 Neutralization loss ratio in the beam extraction and transport region of TCP based RF H<sup>-</sup> ion source.

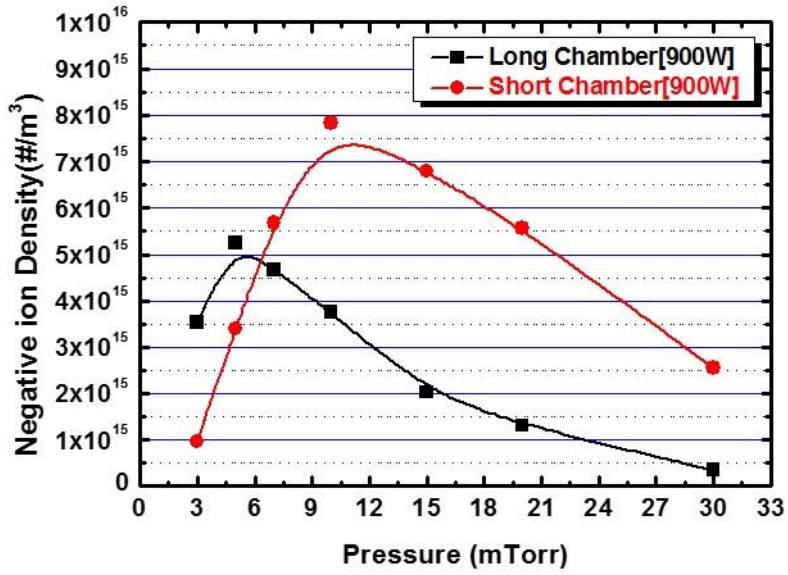


Figure 4.7 Modified H- ion density in consideration of neutralization loss in the H- ion beam transport.

and measured the accelerated beam transport region as shown in Fig. 4.4. The loss rate of the H- beam passing through the extraction length of 3 cm can be calculated as following.

$$I = I_0 \exp[-\sigma_{H_2, \text{det}} nL]$$

where  $I_0$  is initial beam current,  $\sigma_{H_2, \text{det}}$  is neutralization cross-section of H- ion by hydrogen molecules and  $n$  is the hydrogen neutral density. Figure 4. 5. shows the neutralization ratio as a function of pressure at the 3cm extraction region and 30cm beam transport region. Fig. 4. 6 shows the calculated loss rate at the extraction region and transport region using actual measured plasma parameter shows that the loss rate at the extraction region can be 10~70 % when operating pressure varies from 3 to 30 mTorr though the traveling length is short, but the beam loss at the transport region is less than 10% even with the longer beam transport length as shown in figure 4. 7. Therefore the loss at the extraction region is much significant that that at the transport region. The expected H- density at the extraction hole has been calculated using measured H- density at the position 1 cm away from extraction hole and the calculated loss rate and shows similar tendency to the extracted beam current.

#### 4.3.2 Effects of magnetic filter field structure in the H- ion source region

Although the neutralization loss of H- ion beam explains reduced beam current in the higher operating pressure for both chamber length configurations, the higher H- ion beam current with short chamber in the low operating pressure still shows difference in compared to the result of the measured H- ion density. Therefore, additional production and destruction processes of H- ion are investigated between the measuring position and the extraction hole region, since The H- density is measured at the position 1 cm away from the extraction hole.

In consideration of volume production of H<sup>-</sup> ions, the reduction of electron temperature at the extraction region is the important condition, and increasing rate of H<sup>-</sup> ion is highly depends on the reduction of electron temperature as already described in the chapter 3. The reduction of electron temperature comes from the different loss rate of energetic electrons along the transverse magnetic field. The high energy electron fast diffuses along the magnetic field line and get lost to the wall while low energy electrons can diffuse across the magnetic field by collisions with neutrals due to the relatively shorter diffusion time along magnetic field than high energy electrons. Therefore the reduction of electron temperature under filter magnetic field depends on not only the strength of magnetic filter field but also the length of filter magnetic filter field region which is represented to  $\int B \cdot dl$ . [39] As shown in figure 4.8, the filter magnetic field strength becomes higher as the position gets closer to the extraction hole. Therefore, plasma parameters can change drastically near the extraction hole even for the short transport distance as 1cm between the measuring position and the extraction hole region. Consequently, the measured plasma parameters has been analyzed as a function of  $\int B \cdot dl$  value to estimate plasma parameters near the extraction hole region. As shown in figure. 4.9 and 10, the electron density remain rather constant but electron temperature has clear decreasing tendency with higher  $\int B \cdot dl$  value for the change of magnetic filter field strength. In addition, the electron temperature is sufficiently low with long chamber and higher  $\int B \cdot dl$  value, therefore further decrease of electron temperature is not plausible compared to the short chamber configuration. Based on the characteristics of electron density and temperature for the both chamber configurations, the H<sup>-</sup> ion density is compared for  $\int B \cdot dl$  value. As shown in Fig. 4. 11, higher increase rate of H<sup>-</sup> ion density at low operating pressures with the long chamber configuration for larger  $\int B \cdot dl$  value, indicating more electron temperature decrease. Therefore, similar drastic increase of H<sup>-</sup> ion density in the

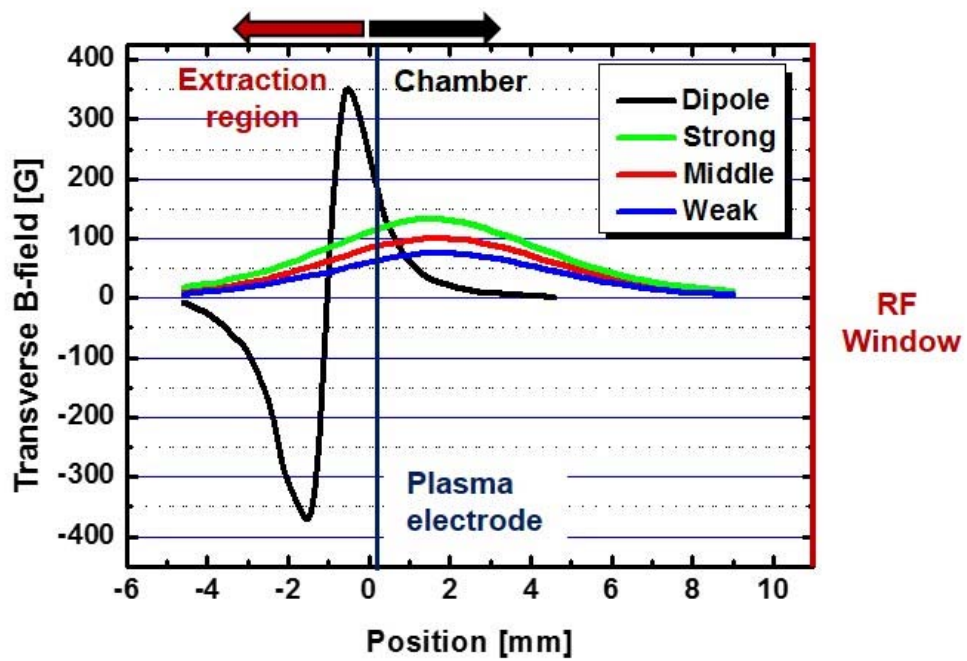


Figure 4.8 Calculated axial transverse magnetic field profile in the source region.

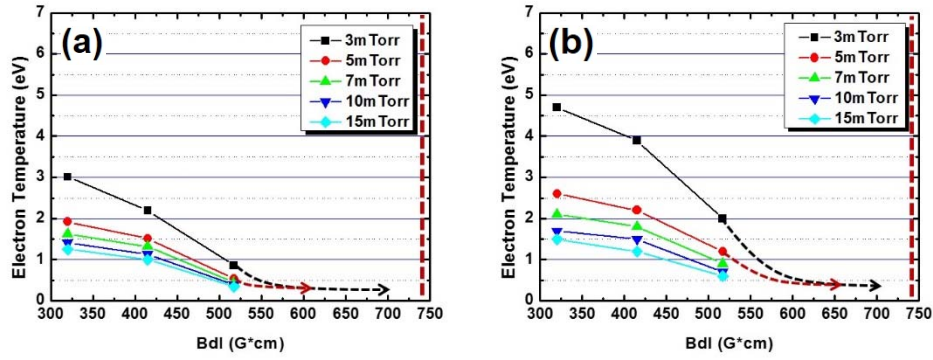


Figure 4.9 Characteristics of electron temperature for various  $\int B \cdot dl$  value with (a) long chamber, (b) short chamber configuration.

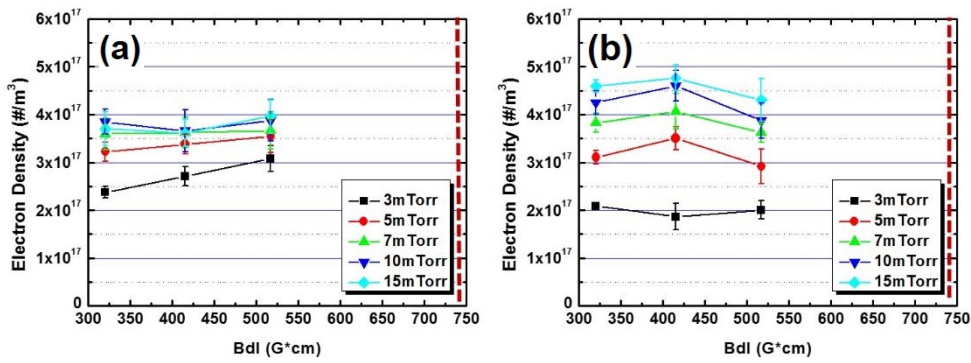


Figure 4.10 Characteristics of electron density for various  $\int B \cdot dl$  value with (a) long chamber, (b) short chamber configuration.

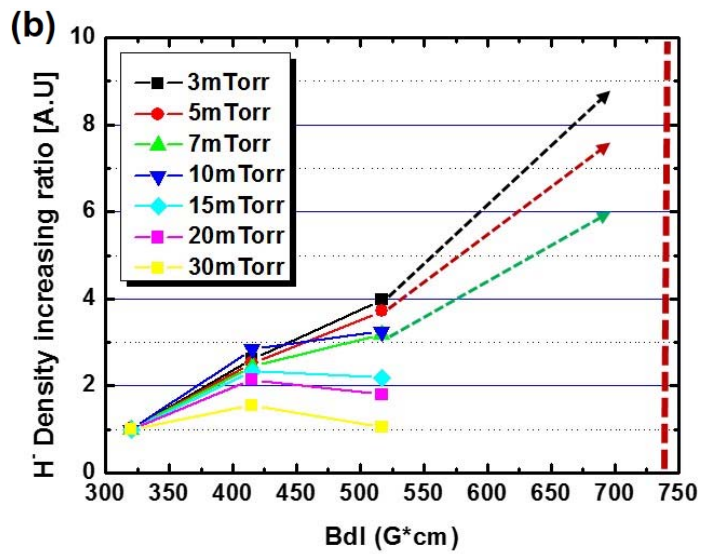
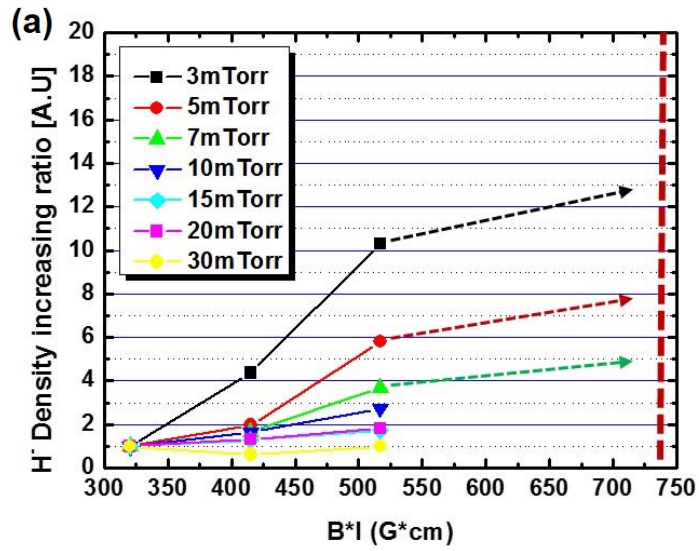


Figure 4.11 H<sup>+</sup> ion density increasing ratio for various  $\int B \cdot dl$  value with (a) long chamber (b) short chamber.

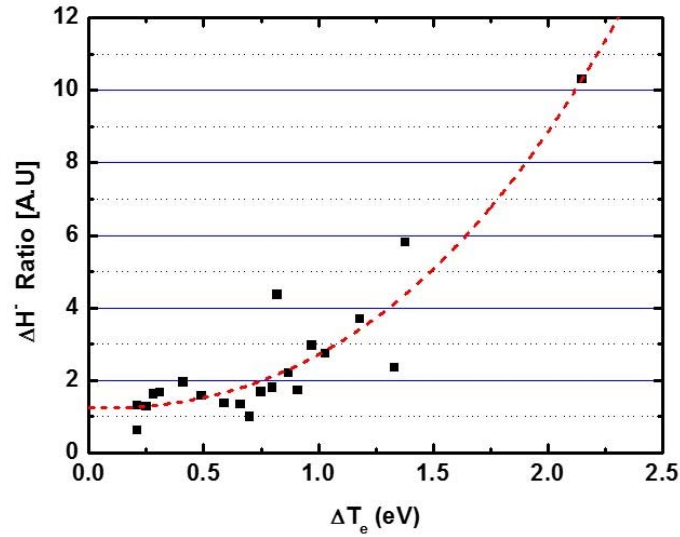


Figure 4.12 Increase rates of H- ion density as a function of the reduced electron temperature.

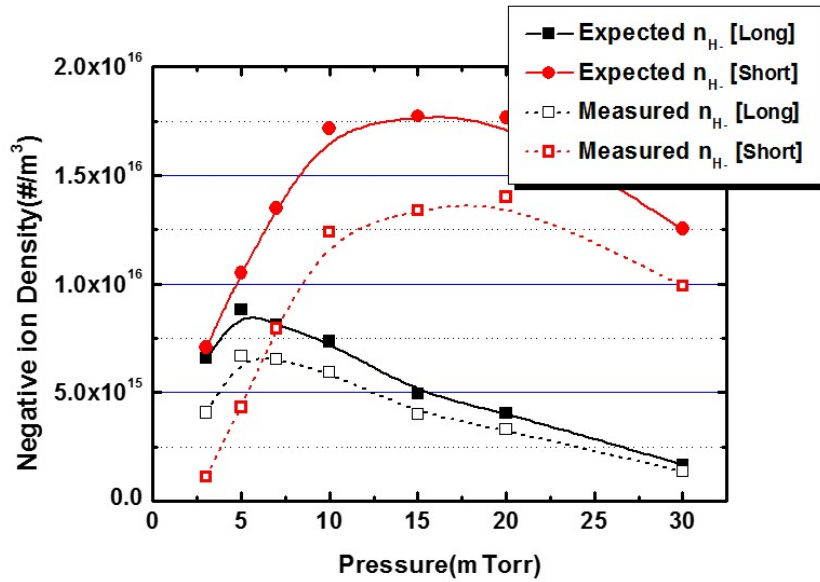


Figure 4.13 Estimation of H- ion density near the extraction hole region.

lower operating pressure regime is also expected with the short chamber configuration due to further temperature drop when additional filtering for the travel of 1cm in front of the extraction hole is accounted for. Moreover, saturated low electron temperature at high pressures gives no further increase with additional filter region in front of the extraction hole for both configurations. From these results, increase rates of H- ion density can be approximated as quadratic function of the decrease of electron temperature in the extraction region as shown in Fig. 4.12. Based on the increase rate of the long chamber configuration, changes of H- ion density for both chamber configurations are estimated by accounting additional temperature drops from the 1cm in front of the extraction hole as shown in Fig. 4.13. This result well explain the higher H- ion beam current in the low operating pressure with short chamber and indicates that high  $\int B \cdot dl$  value is more suitable to suppress electron temperature operating at low pressure regime.

In addition to the production of the H- ions in the transport region, the H- ions can be lost during the transport inside the ion source. The loss rate of H- ions by traveling 1cm to the extraction hole has been calculated. The mean free path of H- ion has been calculated as following equations considering the destruction reaction rates of H- ion by H<sup>+</sup> and H atom and electron.

$$\lambda_{H \text{ det}} = \frac{v^-}{n_H \langle \sigma v_H \rangle}, \quad \lambda_{MN} = \frac{v^-}{n_{H^+} \langle \sigma v_{H^+} \rangle}, \quad \lambda_{ED} = \frac{v^-}{n_e \langle \sigma v_e \rangle}$$

where  $\lambda_{MN}$  is mean free path of the H- ion for destruction in collision with the positive H ions,  $\lambda_{H \text{ det}}$  with H atoms, and  $\lambda_{ED}$  with electrons.  $v^-$  is the thermal velocity of the H- ion assuming 0.1 eV of H- ion temperature[ ]. Basically, this equations indicate that the mean free path gets shorter as the electron temperate decreases, and as electron density increases. Figure 4. 14. shows the mean free path by destruction reactions with short chamber and 900 W RF power in the large

$\int B \cdot dl$  configuration. As expected when the operating pressure is higher, the electron temperature is relatively lower therefore mean free path of destruction process by electron is relatively longer as well, but when operating pressure is lower and electron temperature is relatively higher the mean free path of destruction process by electron is shorter. However as operating pressure get higher and the electron density is sufficiently large, the mean free path also gets shorter.

The total mean free path based on the mean free path by each reaction can be expressed as following.

$$\lambda_c = \left( \frac{v^-}{n_H \langle \sigma v_e \rangle} + \frac{v^-}{n_{H^+} \langle \sigma v_e \rangle} + \frac{v^-}{n_e \langle \sigma v_e \rangle} \right)^{-1}$$

As shown in figure 4.15, the loss rate of 1cm traveling length is estimated to be 10~20% for both chamber length. From this result, as the electron temperature at the extraction region can be low enough and high electron density can be achieved at high pressure regime. Therefore relatively low  $\int B \cdot dl$  value is more effective to enhance  $H^-$  beam current in considering transport loss of the volume produced  $H^-$  ions in the magnetic filter field region.

Consequently,  $H^-$  ion beam current and modified  $H^-$  ion density in considering additional  $H^-$  ion production and destructions as shown in Fig. 16 is quite well matched. In addition, result of the  $e/H^-$  ratio from the  $H^-$  ion beam current and measured  $H^-$  ion density also show similar tendency as shown in Fig. 4.17. Therefore, it is concluded that  $H^-$  ion beam current in the volume-produced  $H^-$  ion source can be optimized depending on the operating pressure regime by not only reducing electron temperature in the extraction region with higher magnetic filter field but also adjusting  $\int B \cdot dl$  value to increase  $H^-$  ion production in considering plasma parameters.

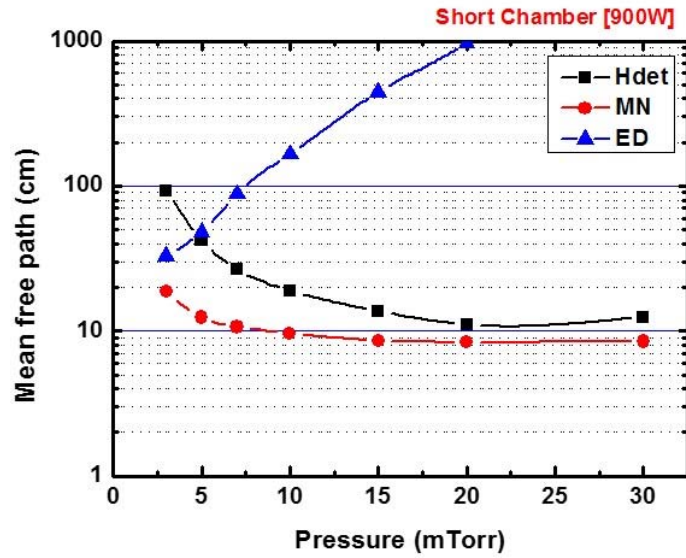


Figure 4.14 Calculated mean free path for H<sup>-</sup> ion destruction reactions.

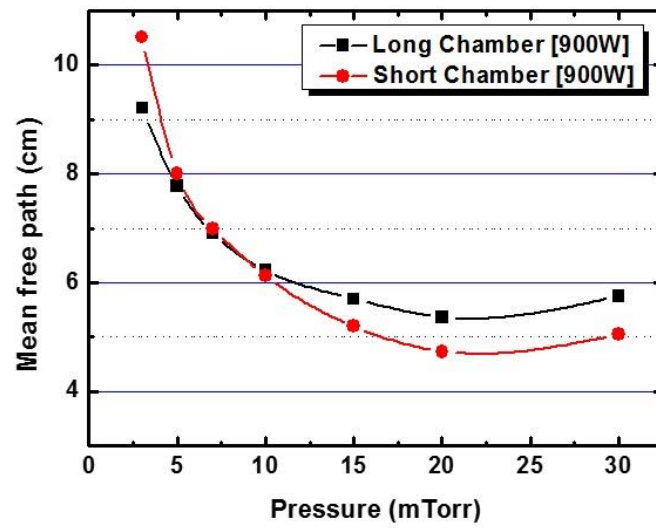


Figure 4.15 Calculated mean free path for total H<sup>-</sup> ion destruction reactions.

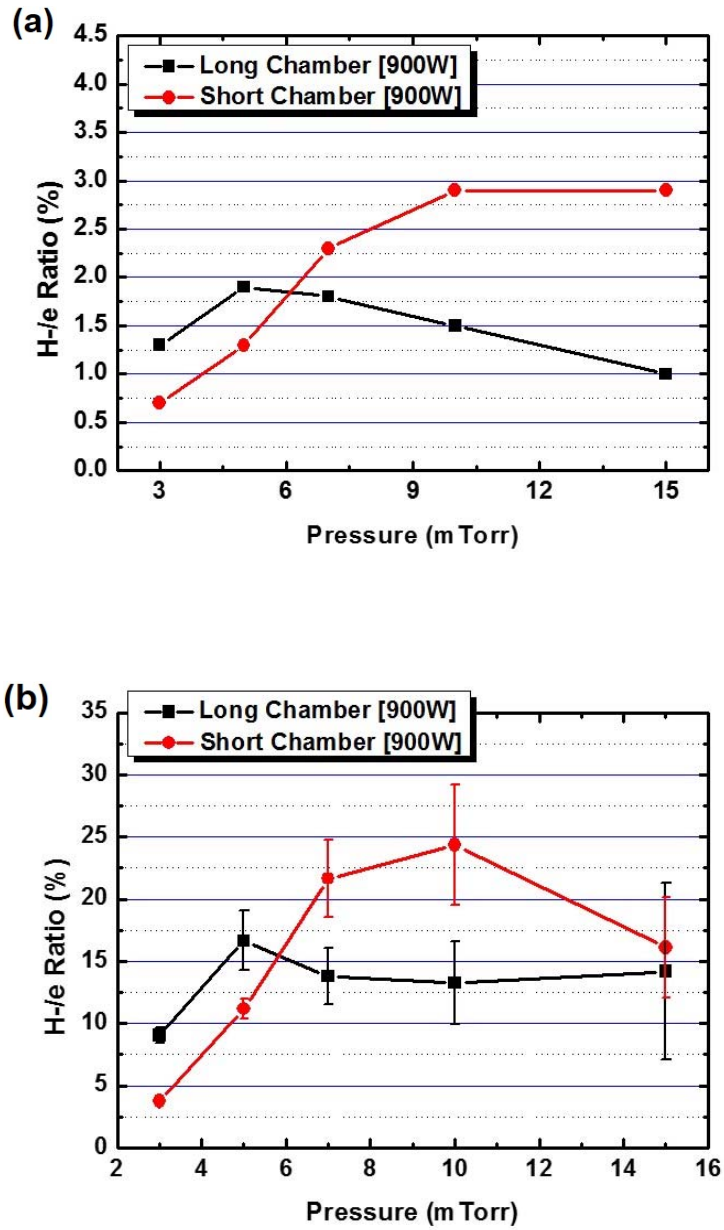


Figure 4.16 Comparison of  $e/H^-$  ratio between the results from (a) the measured  $H^-$  ion density and (b) the  $H^-$  ion beam current.

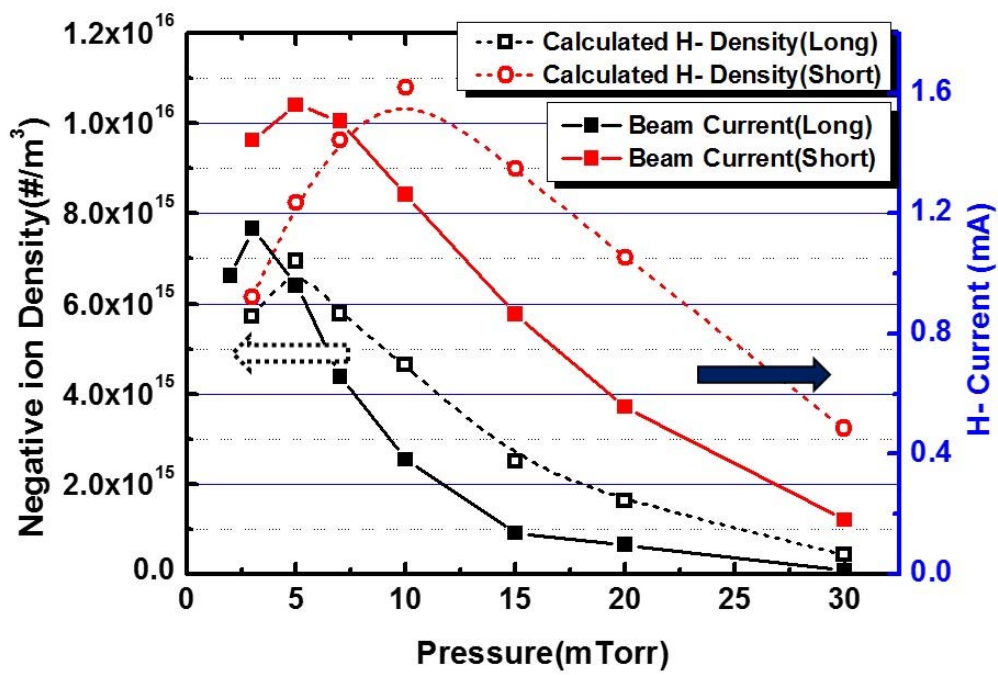


Figure 4.17 Comparison of H- ion beam current with modified H- ion density in considering additional H- ion production and destructions.

## Chapter 5 Summary and Conclusion

In this research, it is newly suggested that the reduced effective plasma size significantly increases  $H^-$  ion production via the increase of electron temperature in volume-produced  $H^-$  ion sources. Almost 50% increase in the electron temperature is achieved by shortening the chamber length from 11 cm to 7.5 cm (30% reduction).  $H^-$  ion density measurement with laser photo-detachment in the short chamber shows a few times increase compared to the longer one at the same heating power depending on gas pressure. Moreover, increase of extracted  $H^-$  ion beam current up to 1.45 mA at RF power of only 0.9 kW (3.2 mA/cm<sup>2</sup>/kW) is successfully achieved, which is comparable to the highest  $H^-$  current density per unit RF power of the established major volume-produced  $H^-$  ion sources. It is noteworthy in terms that beam current enhancement is achieved only by changing the chamber geometry without providing additional heating power. However, the measured  $H^-$  ion density is observed to decrease in low pressure regime with the small effective plasma size configuration due to the increase of electron temperature in the extraction region along with the driver region. Therefore, it is recognized that the structure of magnetic filter field should also be modified in accordance with the modified plasma characteristics due to the change of chamber geometry.  $H^-$  ion density measurement carried out with laser photo-detachment for various strengths of magnetic filter field shows that the increase rate of  $H^-$  ion density is highly dependent on the reduced electron temperature in the extraction region.

In addition, it is observed that higher  $H^-$  ion beam current is extracted in low operating pressure regime down to 3 mTorr even though the  $H^-$  ion density is measured to be lower in this regime due to insufficient filtering of high energy electrons at the extraction region. This discrepancy can be explained by the change

of plasma parameters between the measuring position and the extraction hole region due to additional filtering during the transport in front of the extraction hole in terms of  $\int B^* dl$  value. Based on the increase rate of  $H^-$  ion density as a function of the reduced electron temperature, changes of  $H^-$  ion density for both chamber configurations are estimated by accounting additional temperature drops from the 1 cm in front of the extraction hole. Taking this effect into account, further increase of  $H^-$  ion density with the short chamber can be expected due to more reduction of electron temperature than the longer one at the same  $\int B^* dl$  value. This result well explains the higher  $H^-$  ion beam current in the low operating pressure with short chamber and also indicates that high  $\int B^* dl$  value is more suitable to suppress high energy electrons for operation at low pressure regime. On the contrary, the electron temperature at the extraction region can be low enough and high electron density can be achieved at high pressure regime. In this operating regime, calculation of mean free path for the  $H^-$  ion destruction reveals that the main destruction process during the transport of  $H^-$  ions in source region is the mutual neutralization reaction which is proportional to the electron density. Therefore, relatively low  $\int B^* dl$  value is more effective to enhance  $H^-$  beam current in considering transport loss of the volume-produced  $H^-$  ions across the magnetic filter field region. It is concluded that  $H^-$  ion beam current in the volume-produced  $H^-$  ion source can be optimized depending on the operating pressure regime not only by reducing the electron temperature in the extraction region with higher magnetic filter field but also by adjusting  $\int B^* dl$  value with consideration of plasma parameters to increase  $H^-$  ion production.

In this dissertation, the discharge chamber and magnetic filter field configuration as the  $\int B^* dl$  value are proposed as critical design parameters from the effects on the RF plasma parameters to increase volume-produced  $H^-$  ion density. Moreover, it has been confirmed that the performance of the volume-

produced  $H^-$  ion source at a given operating pressure and RF power condition can be optimized by controlling plasma parameters with changing discharge chamber geometry and  $\int B \cdot dl$  value depending on the operating pressure.

## References

- [1] D. P. Moehs, J. Peters, and J. Sherman, IEEE Transactions on Plasma Science, **33**, 6, 1786, (2005).
- [2] R. S. Hemsworth, and T. Inoue, IEEE Transactions on Plasma Science, **33**, 6, 1799 (2005).
- [3] M. Muramatsu, and A. Kitagawa, Rev. Sci. Instrum. **83**, 02B909, (2012).
- [4] G.I. Dimov, Rev. Sci. Instrum., **67**, 3393, (1996).
- [5] ‘Progress in the ITER Physics Basis’, Nucl. Fusion, **47**, S1, (2007).
- [6] R. Hemsworth, H. Decamps, J. Graceffa, B. Schunke, M. Tanaka, M. Dremel, A. Tanga, H.P.L. De Esch, F. Geli, J. Milnes, T. Inoue, D. Marcuzzi, P. Sonato and P. Zaccaria, Nucl. Fusion, **49**, 045006, (2009).
- [7] H.P.L. De Esch et al., Fusion Engineering and Design, **26**, 589, (1995).
- [8] T. Inoue et al., Fusion Engineering and Design **56**, 517, (2001).
- [9] W. Kraus et al., Rev. Sci. Instrum. **83**, 02B104, (2012).
- [10] M. Bacal, A. Hatayama, and J. Peters, IEEE Transactions on Plasma Science **33**, 6, 1845, (2005)
- [11] M. Bacal, Chemical Physics, **398**, 3, (2012).
- [12] R. Janev, D. Reiter, and U. Samm, Collision processes in low-temperature hydrogen plasmas, Report Jül-4105, Forschungszentrum Jülich, Germany (2003).
- [13] S. Waltner, K. N. Leung, W. B. Kunkel, J. Appl. Phys., **64**, 3424, (1988).
- [14] K. N. Leung, S. Waltner, W. B. Kunkel, Phys. Rev. Lett., **62**, 764, (1989).
- [15] M. Bacal, Nucl. Fusion, **46**, S250, (2006).
- [16] M. Bacal, Rev. Sci. Instrum., **79**, 02A516, (2006).
- [17] J. R. Hiskes, J. Appl. Phys., **51**, 4592, (1980).
- [18] J. Lourerio, C. M. Ferreira, J. Phys. D: Appl. Phys., **56**, 1927, (1984).
- [19] J. R. Hiskes, A. M. Karo, J. Appl. Phys., **56** S1 (2007).
- [20] D. Rapp, P. Englander-Golden, J. Chem. Phys., **43**, 1464, (1965).

- [21] M. Cacciatore et. al., J. Phys. D: Appl. Phys., **13**, 575, (1980).
- [22] M. A. Khakoo et. al., J. Phys. B: At. Mol. Opt. Phys., **27**, 2355, (1994).
- [23] D. T. Stibbe et. al., New J. Phys., **1**, 2.1-2.9, (1998).
- [24] J. R. Hiskes, A. M. Karo, J. Appl. Phys., **56**, 1972, (1984)
- [25] M. Bacal, A. M. Bruneteu, W. G. Graham, G. W. Hamilton, and M. Nachman, J. Appl. Phys., **52**, 1247 (1981).
- [26] M. Bandyopadhyay, PhD dissertation, Technical University of Munich, (2004).
- [27] H. S. Jeong, Master thesis, Seoul National University, (2006).
- [28] Y. H. An et. al., Rev. Sci. Instrum., **77**, 3 (2012)
- [29] M. A. Lieberman and A. J. Lichtenberg, Principles of Plasma Discharges and Material Processing. (Wiley, Hoboken, New Jersey, ed. 2nd, 2005).
- [30] R. Zorat, Plasma Sources Sci. Technol. **9**, 161 (2000).
- [31] Huba J D 1998 Revised NRL Plasma Formulary p 39.
- [32] J. R. Roth, Industrial Plasma Engineering: vol. 1. Principles. (Institute of Physics Publishing, Bristol and Philadelphia, 1995).
- [33] F. F. Chen, "Langmuir probe analysis for high density plasmas," Physics of Plasmas **8** (6), 3029 (2001).
- [34] D. N. Ruzic, Electric Probes for Low Temperature Plasmas. (AVS Press, New York, 1994).
- [35] M. Bacal, P. Berlemont, A. M. Bruneteau, R. Leroy, and R. A. Stern, J. Appl. Phys., **70**, 1212, (1991).
- [36] F. El BalghitiSube, F. G. Baksht, and M. Bacal, Rev. Sci. Instrum., **67**, 2221 (1996).
- [37] S Christ-Koch, U Fantz, M Berger and NNBI Team, Plasma Sources Sci. Technol., **18**, 025003, (2009).
- [38] Lebedev V, Presnyakov L and Sobel'man I 2000 JETP Lett., **72**, 178, (2000).
- [39] M. Nishiura, M. Sasao, and M. Bacal, J. Appl. Phys. **83**, 2944 (1998).
- [40] H. Zhang, Ion sources, Springer (1999).
- [41] P. Franzen, L. Schiesko, M. Froschle, D. W. Underlich, U Fantz and the NNBI Team, Plasma Phys. Control. Fusion, **53**, 115006, (2011).

## Abstract in Korean

# 체적 생성 RF 수소 음이온원의 효율적인 운전을 위한 플라즈마 변수 제어에 관한 연구

정 봉 기

에너지시스템공학부

(원자핵공학 전공)

서울대학교 대학원

고주파(Radio-frequency) 플라즈마를 이용한 체적 생성 수소 음이온원은 세슘을 사용하는 표면 생성 수소 음이온원에 비해 장시간 운전에서 높은 안정성을 가진다. 하지만 다양한 수소 음이온원 응용에서 요구하는 조건을 만족하기 위해서는 더욱 낮은 입력 파워 및 운전 압력 조건에서 보다 높은 음이온 빔 전류 밀도를 달성해야 한다. 일반적으로 수소 음이온의 체적 생성을 증가시키기 위해서는, 전체적인 플라즈마 영역에서 높은 전자 밀도를 유지하면서, 구동 영역의 높은 전자 온도를 달성하고 음이온 인출 영역의 전자 온도를 낮은 상태로 유지하는 것이 필수적이다. 인출 홀 근처 필터 자기장에 의한 전자 온도 감소에 대한 실험 결과들은 잘 알려진 반면에, 구동 영역의 전자 온도를 증가시키기 위한 방법으로, 고주파 파워 증가 및 구동 주파수 변화 등이 시도되었지만 전자 밀도의 증가를 이끌어내는데 그치고 전자 온

도의 향상은 미비하였다. 따라서, 본 연구에서는 수소 플라즈마의 입자 균형 모델에서 설명되는 전자온도에 대한 특성을 바탕으로, 주어진 운전 압력 조건에서 플라즈마 체적과 유효 면적간의 비율로 나타내어지는 유효 플라즈마 크기(effective plasma size)를 변화시켜 구동 영역 온도를 제어 하는 방법을 제안하고, 실제 수소 음이온원의 방전 챔버의 길이를 조절하는 형태로 적용하여 그 효과에 대한 연구를 진행하였다.

고주파 보상 랑뮈어 탐침(Langmuir Probe) 측정 결과, 방전 챔버의 길이를 감소시켜 유효 플라즈마 크기가 작아졌을 때, 동일한 운전 압력 및 입력 파워 조건에서 구동 영역의 전자 온도가 급격하게 증가하는 것이 확인되었으며, 레이저 광전자 탈리(laser photo-detachment) 측정 방법을 통해 얻어진 인출 영역의 수소 음이온 밀도 값 또한 최적 압력 조건에서 3~4배 정도 증가하는 것을 확인하였다. 하지만 운전 압력이 낮아짐에 따라, 작은 유효 플라즈마 크기 조건에서 음이온 밀도 값이 급격하게 감소하는 것을 볼 수 있었고, 이는 구동영역의 전자온도가 증가함에 따라 인출 영역의 전자 온도 또한 증가하게 되어 음이온 생성 반응이 줄어드는 것으로 설명 할 수 있었다. 따라서, 인출 영역의 전자온도를 제어하기 위한 필터 자기장의 세기에 대한 연구를 진행하여, 기본적으로 구동 영역의 전자 온도가 증가할 경우 필터 자장의 크기를 증가시켜야만 인출 영역 전자온도를 충분히 낮은 상태로 유지할 수 있으며 수소 음이온 밀도 또한 높아지는 것을 확인하였다. 결과적으로 운전 압력과 유효 플라즈마 크기를 제어하여 구동 영역의 전자온도를 효율적으로 높이고 필터 자장의 세기를 증가시켜 인출 영역의 전자온도를 충분히 감소시켰을 때, 높은 체적 생성 수소 음이온 밀도를 달성할 수 있음을 알았다.

이러한 연구를 바탕으로 방전 챔버의 길이를 줄이고, 인출 영역의 필터 자장의 세기를 증가시킨 결과, 900W의 동일한 고주파 파워를 사용했을 때 기존보다 30% 증가한 1.45 mA의 수소 음이온 빔 전류를 인출하였다. 이는 3.2 mA/cm<sup>2</sup>/kW의 입력 파워당 빔 전류 밀도 값으로,

현재 보고된 고주파를 이용한 체적 수소 음이온원 중 가장 높은 성능을 가지는 장치의 값과 동일한 수준임을 알 수 있었다. 또한, 방전 챔버 길이를 줄였을 경우, 낮은 압력 영역에서는 상대적으로 높은 인출 영역 전자 온도로 인해 측정된 음이온 밀도가 기존 챔버 길이의 결과보다 낮았으나, 인출된 빔 전류의 경우에는 낮은 압력 조건임에도 불구하고 빔 전류 값이 더 높은 것을 알 수 있었다. 이는 측정 위치에서 인출 홀까지의 필터 자장 세기 및 영역에 대한 값으로 나타내어지는  $\int B \cdot dl$  값의 증가를 고려할 때, 짧은 길이의 챔버를 사용한 조건에서 전자 온도 감소량이 커지고, 인출 홀 근처에서 음이온 밀도 값이 상대적으로 크게 증가하여 빔 전류 값이 증가하는 것으로 설명할 수 있다. 이는 작은 유효 플라즈마 크기와 낮은 운전 압력 조건, 즉 높은 구동 영역 전자 온도 조건에서는 높은  $\int B \cdot dl$  값을 가지는 필터 자장 구조가 전자 온도 감소에 유리하기 때문이다. 이와 반대로, 상대적으로 높은 운전 압력 조건, 즉 인출 부 전자 온도가 충분히 낮고 전자 밀도가 높은 조건일 때는 음이온의 수송에 따른 감소 현상이 증가하게 된다. 따라서 낮은  $\int B \cdot dl$  값을 가지는 구조일 때, 충분한 전자 온도의 감소뿐만 아니라 인출 홀까지의 수송거리가 줄어들어 인출 홀 근처의 높은 음이온 밀도가 음이온 빔 전류의 증가로 이어질 것을 예측할 수 있다. 결과적으로, 단순히 필터 자기장의 세기에 따른 전자 온도 제어만이 아니라, 동일한 유효 플라즈마 크기 조건에서 낮은 운전 압력 조건일 때는 높은  $\int B \cdot dl$  값을 가지는 필터 자기장 구조가 전자 온도를 감소시키는데 유리하고, 높은 압력 조건일 때는 낮은  $\int B \cdot dl$  값을 가지는 필터 자기장 구조가 음이온의 수송에 따른 감소를 최소화하여 더욱 높은 음이온 빔 전류를 인출할 수 있음을 알았다.

본 연구에서는 방전 챔버 구조에 따른 유효 플라즈마 크기와, 자기장 구조에 따른  $\int B \cdot dl$  값이 고주파 플라즈마 변수에 미치는 영향을 바탕으로, 이를 체적 생성 음이온원의 주요 설계 변수로 제시하였다. 또한 주어진 운전 압력 및 파워 조건에 따른 최적화를 통하여 체

적 생성 음이온원의 성능을 효율적으로 개선 시킬 수 있음을 보였다. 이 결과는 기존 체적 생성 수소 음이온원의 성능 개선을 위한 적용뿐만 아니라 장시간 운전을 필요로 하는 수소 음이온원 응용 분야의 적용 확대에도 기여 할 것으로 기대 된다.

주요어 : 체적 생성 수소 음이온원, 플라즈마 변수, 유효 플라즈마 크기, 필터 자장, 음이온 빔 인출

학번 : 2009-30261